



# **JGR** Solid Earth

# <del>-</del>

### RESEARCH ARTICLE

10.1029/2024JB028781

### **Key Points:**

- Upper mantle stratification is constrained using Clean Receiverfunction Imaging using Sparse Radon Filters and machine learning
- Stratification is classified into intralithospheric, transitional and sublithospheric
- High-resolution constraints allow the evaluation of different causal models

### **Supporting Information:**

Supporting Information may be found in the online version of this article.

#### Correspondence to:

S. A. B. Carr, scarr13@ur.rochester.edu

#### Citation:

Carr, S. A. B., & Olugboji, T. (2024). A taxonomy of upper-mantle stratification in the US. *Journal of Geophysical Research: Solid Earth, 129*, e2024JB028781. https://doi.org/10.1029/2024JB028781

Received 19 JAN 2024 Accepted 8 MAY 2024

### **Author Contributions:**

**Data curation:** Steve A. B. Carr **Formal analysis:** Steve A. B. Carr

Funding acquisition: Tolulope Olugboji
Investigation: Steve A. B. Carr
Methodology: Tolulope Olugboji
Project administration:
Tolulope Olugboji
Resources: Tolulope Olugboji
Software: Steve A. B. Carr
Supervision: Tolulope Olugboji
Visualization: Steve A. B. Carr
Writing – original draft: Steve A. B. Carr
Writing – review & editing: Steve
A. B. Carr, Tolulope Olugboji

© 2024. The Author(s).

This is an open access article under the terms of the Creative Commons

Attribution License, which permits use, distribution and reproduction in any medium, provided the original work is properly cited.

# A Taxonomy of Upper-Mantle Stratification in the US

Steve A. B. Carr<sup>1</sup> and Tolulope Olugboji<sup>1,2,3</sup>

<sup>1</sup>Department of Earth and Environmental Sciences, University of Rochester, Rochester, NY, USA, <sup>2</sup>Georgen Institute of Data Sciences, University of Rochester, Rochester, NY, USA, <sup>3</sup>Department of Electrical and Computer Engineering, University of Rochester, Rochester, NY, USA

**Abstract** The investigation of upper mantle structure beneath the US has revealed a growing diversity of discontinuities within, across, and underneath the sub-continental lithosphere. As the complexity and variability of these detected discontinuities increase—for example, velocity increase/decrease, number of layers and depth—it is hard to judge which constraints are robust and which explanatory models generalize to the largest set of constraints. Much work has been done to image discontinuities of interest using S-waves that convert to P-waves (or top-side reflected SS waves). A higher resolution method using P-to-S scattered waves is preferred but often obscured by multiply reflected waves trapped in a shallower layer, limiting the visibility of deeper boundaries. Here, we address the interference problem and re-evaluate upper mantle stratification using filtered P-to-S receiver functions (Ps-RFs) interpreted using unsupervised machine-learning. Robust insight into upper mantle layering is facilitated with CRISP-RF: Clean Receiver-Function Imaging using Sparse Radon Filters. Subsequent sequencing and clustering organizes the polarity-filtered Ps-RFs into distinct depth-based clusters. We find three types of upper mantle stratification beneath the old and stable continental US: (a) intra-lithosphere discontinuities (paired or single boundary), (b) transitional discontinuities (single boundary or with a top layer), and (c) sub-lithosphere discontinuities. Our findings contribute a more nuanced understanding of mantle discontinuities, offering new perspectives on the nature of upper mantle layering beneath continents.

Plain Language Summary Early investigations of the mantle rocks in the US indicate intricate layering. However, uncertainties remain regarding the origins of these structures. Here, we re-examine mantle rock stratification using a fine-resolution approach. We use short waves that improve our ability to identify the depth of thin layers and sharp transitions in rock properties. Until now, these methods haven't been used due to interference with waves trapped in the near-surface layers. We address this problem with machine learning and the CRISP-RF (Clean Receiver Function Images Using Sparse Radon-Filters) method. CRISP-RF filters out the waves trapped in the crust and machine learning reveals spatially coherent patterns. Underneath the stable continents, we find evidence for different types of rock layering: (a) reflectors within cold stiff rocks (b) reflectors at depth ranges where the rocks become warmer and flow more readily, and (c) reflectors at depths farther down in the upper mantle. Our approach enables the test of hypotheses about the origins of upper mantle layering beneath continents.

# 1. Introduction

Seismological constraints on upper mantle layering beneath the contiguous US have revealed evidence for negative and positive velocity discontinuities hinting at a complex layering beneath the continental US (Abt et al., 2010; Hopper & Fischer, 2018; Hua et al., 2023; Kind & Yuan, 2018; L. Liu & Gao, 2018; T. Liu & Shearer, 2021). The mid-lithosphere discontinuities (MLDs) are the most widely detected and are defined by one or more negative velocity gradients confined to depths of 60–170 km (Abt et al., 2010; Hopper & Fischer, 2018; Kind & Yuan, 2018; Krueger et al., 2021; T. Liu & Shearer, 2021). Beneath this discontinuity, within a depth range of 120–220 km, recent, but sporadic detections of positive velocity gradients (PVGs) have been reported and interpreted as the base of the MLDs (Luo et al., 2021). Slightly deeper still, underneath Proterozoic terranes, between 220 and 350 km depth, a negative velocity discontinuity has been detected and attributed to the base of the lithosphere (Mancinelli et al., 2017; Tauzin et al., 2013). These constraints provide improved illumination on the complex layering within the upper mantle beneath the contiguous US; however the interpretations regarding their origins and causes, for example, melt, anisotropy, relics of subduction-related hydration, elastically accommodated grain boundary sliding and metasomatism, are still vigorously debated, confounding a unified model (Ford et al., 2015; Karato, 2012; Rader et al., 2015; Saha et al., 2021; Selway et al., 2015; Wirth & Long, 2014).

CARR AND OLUGBOJI 1 of 23

The most common techniques for imaging the upper mantle discontinuities (UMDs) are long-period body-wave methods: (a) Sp converted waves (Abt et al., 2010; Chen et al., 2018; Hopper & Fischer, 2018; Kind & Yuan, 2018; Krueger et al., 2021) and (b) the top-side S reflections (T. Liu & Shearer, 2021; Shearer & Buehler, 2019). As the data-volume has improved, the earliest observations using Sp converted waves (Abt et al., 2010) have been supplemented by higher resolution studies with more station deployments (Hopper & Fischer, 2018; Kind et al., 2012; Kumar et al., 2012), improved signal-to-noise (Hua et al., 2023; Kind et al., 2020; Krueger et al., 2021) and better depth resolution using S-wave reflections (L. Liu & Gao, 2018; Shearer & Buehler, 2019). Both techniques have identified multiple UMDs within the contiguous US. In the tectonically active western US, a negative discontinuity is unambiguously detected and repeatedly verified by many authors (Abt et al., 2010; Hopper & Fischer, 2018; Kind et al., 2020; Krueger et al., 2021; Kumar et al., 2012; T. Liu & Shearer, 2021). This velocity decrease is inferred to coincide with slow velocities imaged with tomography, and has been interpreted as the boundary between the lithosphere and asthenosphere (Abt et al., 2010; Hansen et al., 2015; Hopper & Fischer, 2018; Kind & Yuan, 2018; Rader et al., 2015). However, this interpretation is inconsistent with the thickness of stable continental lithosphere beneath Archean and Proterozoic terranes in the central and eastern US. Here the velocity decrease is detected at shallower depths (Abt et al., 2010; Hopper & Fischer, 2018; Krueger et al., 2021; T. Liu & Shearer, 2021). This is a distinct discontinuity internal to the lithosphere—the MLD rather than the lithosphere-asthenosphere boundary (LAB) (Abt et al., 2010; Hopper & Fischer, 2018; T. Liu & Shearer, 2021).

To clarify the nomenclature and avoid confusion in our interpretation we define important terms: (a) the thickness of stable continental lithosphere and (b) the depth statistics and polarity of previously detected UMDs. The stable continental lithosphere is that portion of the crust and upper mantle that has remained intact since the Archean and Proterozoic era. Some of its distinct geophysical signatures are: high-velocities, low attenuation, and low heat flow (Dalton et al., 2017; Fischer et al., 2020; Priestley et al., 2018). Its thickness, as inferred from seismology and petrology, extends to a depth ~200-250 km depth (Carlson et al., 2005; Dziewonski & Anderson, 1981; Gung et al., 2003). The seismic detection of a sharp boundary with the asthenosphere in this region is elusive, in contrast with the tectonically active regions (Eaton et al., 2009). This suggests that the bottom boundary of the stable continental lithosphere is marked by velocity gradients that are broad (Mancinelli et al., 2017). Second, we categorize the previously detected UMDs into three groups without any biasing interpretation on their tectonic location or the rheological strength of the rock, that is lithosphere or asthenosphere (Figures 1b-1d). The first group (UMD1) is characterized by a velocity decrease, and typically detected at consistent depths (83  $\pm$  28 km). The second group (UMD2) are positive velocity discontinuities that are slightly deeper (150  $\pm$  30 km), often referred to as the PVG-150 (Hua et al., 2023). The last and final group (UMD3) are deeper negative reflectors (>110 km) that are sporadically detected in some studies (Ford et al., 2015; Kind et al., 2020; T. Liu & Shearer, 2021) and deeper than their shallower counterpart.

Before evaluating which of the earlier mentioned proposed models of upper mantle structure is most consistent with the growing observations, we point out that some authors (Kind et al., 2020) have raised doubts on whether the shallowest and most prevalent discontinuity, UMD1, exists as a real geological feature, especially underneath stable continents. They argued that these discontinuities could be artifacts from the signal processing with no real geological basis (Kind et al., 2020). On the contrary, (Krueger et al., 2021) provide compelling evidence for its visibility within cratons globally. This they do by reprocessing data with rigorous data selection and robust signal processing. Apart from the details of signal processing, some of the differences in observation may be due, in part, to the varying sensitivity and data quality of different imaging techniques as well as the spatial heterogeneity of these discontinuities. One way to address these short-comings is to improve spatial resolution by using shortperiod high-resolution converted or reflected body-waves (Ford et al., 2016; Guan & Niu, 2017; Luo et al., 2021; Pugh et al., 2021; Rychert et al., 2007; Wirth & Long, 2014). However, only a few observations use short-period body waves to image the upper mantle (Ford et al., 2016; Guan & Niu, 2017; Luo et al., 2021; Rychert et al., 2007; Wirth & Long, 2014). Since the long-period body waves (e.g., Sp-RFs and S-reverberations) are often processed at frequencies less than 0.5 Hz, it means that our insight into mantle layering is filtered through a low-resolution lens (Shearer & Buehler, 2019). This limits the resolution on sharpness and ultimately the robustness of interpretations of UMD depths, sharpness, and origins (mantle composition and dynamics).

Here, we achieve improved vertical resolution by utilizing Ps-converted waves processed at a frequency higher than Sp-RFs or S-reflections. However, when using converted Ps waves to detect UMDs, crustal reverberations generated at shallower boundaries like the Moho cause unwanted interference (Abt et al., 2010; Kind et al., 2012;

CARR AND OLUGBOJI 2 of 23

21699356, 2024. 5, Downloaded from https://agupubs.onlinelibrary.wiley.com/doi/10.1029/2024JB028781 by University Of Rochester, Wiley Online Library on [05/09/2024]. See the Terms and Conditions (https://onlinelibrary.wiley.com/doi/10.1029/2024JB028781 by University Of Rochester, Wiley Online Library on [05/09/2024]. See the Terms and Conditions (https://onlinelibrary.wiley.com/doi/10.1029/2024JB028781 by University Of Rochester, Wiley Online Library on [05/09/2024]. See the Terms and Conditions (https://onlinelibrary.wiley.com/doi/10.1029/2024JB028781 by University Of Rochester, Wiley Online Library on [05/09/2024]. See the Terms and Conditions (https://onlinelibrary.wiley.com/doi/10.1029/2024JB028781 by University Of Rochester, Wiley Online Library on [05/09/2024]. See the Terms and Conditions (https://onlinelibrary.wiley.com/doi/10.1029/2024JB028781 by University Of Rochester, Wiley Online Library on [05/09/2024]. See the Terms and Conditions (https://onlinelibrary.wiley.com/doi/10.1029/2024JB028781 by University Of Rochester, Wiley Online Library on [05/09/2024]. See the Terms and Conditions (https://onlinelibrary.wiley.com/doi/10.1029/2024JB028781 by University Of Rochester, Wiley Online Library on [05/09/2024]. See the Terms and Conditions (https://onlinelibrary.wiley.com/doi/10.1029/2024JB028781 by University Of Rochester, Wiley Online Library on [05/09/2024]. See the Terms and Conditions (https://onlinelibrary.wiley.com/doi/10.1029/2024JB028781 by University Of Rochester, Wiley Online Library on [05/09/2024]. See the Terms and Conditions (https://onlinelibrary.wiley.com/doi/10.1029/2024JB028781 by University Of Rochester, Wiley Online Library on [05/09/2024]. See the Terms and Conditions (https://onlinelibrary.wiley.com/doi/10.1029/2024JB028781 by University Of Rochester, Wiley Online Library on [05/09/2024]. See the Terms and Conditions (https://onlinelibrary.wiley.com/doi/10.1029/2024JB028781 by University Of Rochester, Wiley Online Library.wiley.

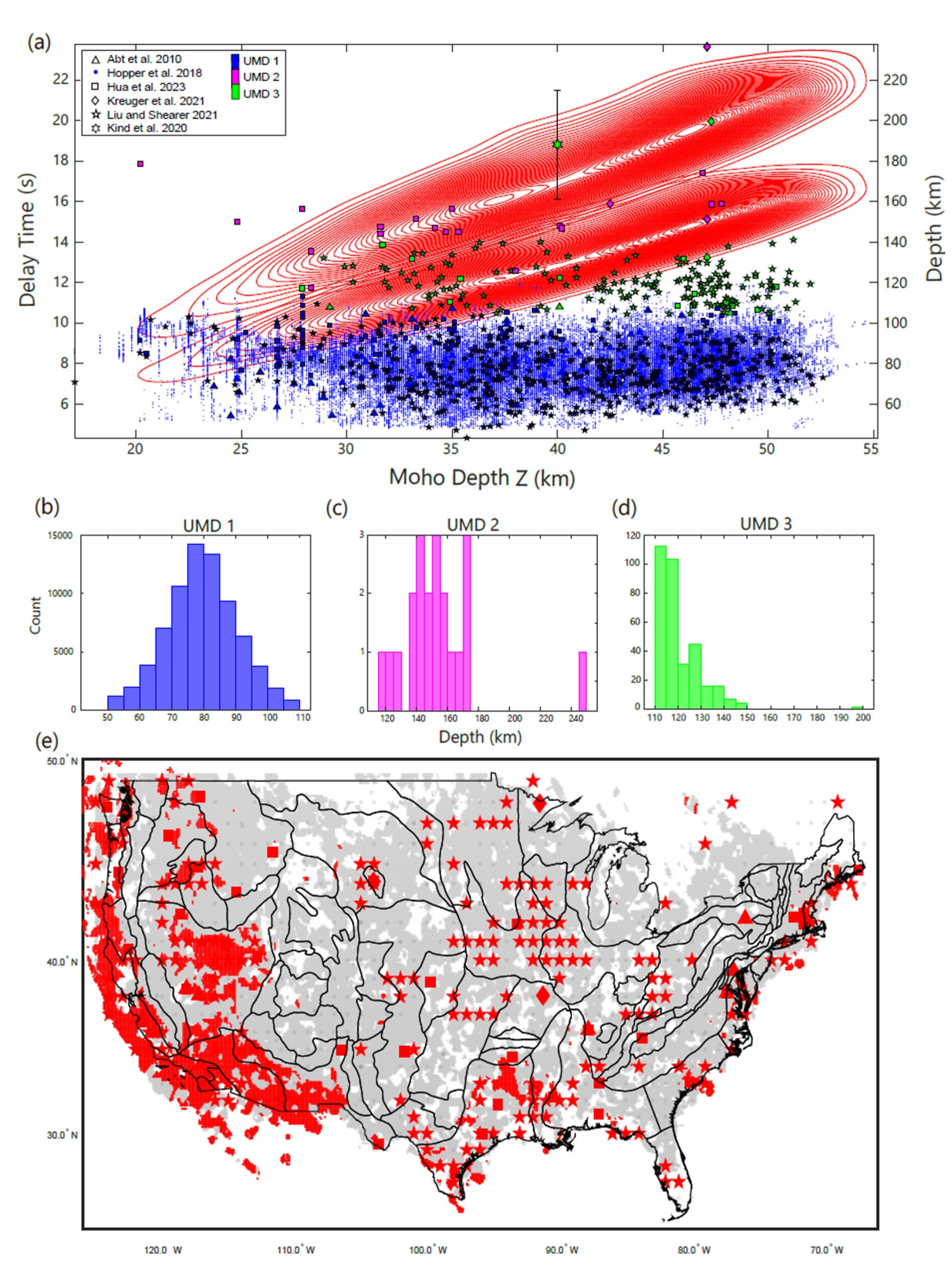


Figure 1.

CARR AND OLUGBOJI 3 of 23

Olugboji, Zhang, et al., 2023). This confounds the interpretation of deeper mantle discontinuities. We illustrate this by comparing the UMD arrival times with that calculated for waves reverberated in the crust (red clouds in Figures 1a and 1e). We use a continental Moho model from Schmandt et al. (2015), and crustal velocities from Shen and Ritzwoller (2016). We observe that several UMDs reported in earlier studies (Abt et al., 2010; Hopper & Fischer, 2018; Kind & Yuan, 2018; Krueger et al., 2021; T. Liu & Shearer, 2021) coincide with Moho multiples. In regions with thick crust, the deeper lithospheric discontinuities (UMD2 and UMD3) are more likely to suffer interference. Even the shallow discontinuity (UMD1) can be affected in areas with a thin crustal layer where short reverberation paths allow multiples to arrive at similar times. Therefore to make P-to-S receiver functions (Ps-RFs) suitable for mantle imaging we require techniques that can isolate mantle conversions from Moho multiples that arrive at similar times. To address this issue, which has long been a challenge in global geophysics, we employ the novel CRISP-RF technique (Clean Receiver-Function Imaging using Sparse Radon Filters) (Olugboji, Zhang, et al., 2023). This method leverages sparsity-promoting Radon transforms to effectively model and isolate mantle-converted energy from crustal multiples (Olugboji, Zhang, et al., 2023).

In the rest of this paper, we describe how we improve our understanding of upper mantle layering in the continental US by analyzing body-wave conversions free of crustal reverberations and noise. We process a large data set by scanning all available data across the contiguous US. We then apply CRISP-RF processing to produce high-resolution, multiple-free Ps-RFs. This enables tighter constraints on discontinuity depth and sharpness. We organize the filtered Ps-RFs into depth-dependent clusters based on an unsupervised machine learning algorithm: a hybrid of the Sequencer and hierarchical clustering algorithm (Baron & Ménard, 2020). This process is crucial for revealing coherent and striking patterns in the data-space of body-wave conversions. We discuss the new insight into upper mantle stratification revealed by our filtered and ordered Ps converted waves: (a) tighter estimation of the depth and polarity of mantle discontinuities, (b) improved visibility of discontinuities across and beneath the stable continental lithoshere, (c) detection of mantle layering with a top and bottom-boundary and the estimation of its thickness (d) a preliminary evaluation of proposed models to explain upper mantle stratification, that is, melt, metasomatism, and elastically accommodated grain-boundary sliding.

### 2. Data

We download and process three-component earthquake waveforms from the Incorporated Research Institution for Seismology (IRIS) database. The majority of the waveforms were recorded by stations that are part of the Transportable Array (TA) with additional contributions from all the major regional seismic networks within the contiguous US. The initial waveform database comprised ~500, 000 earthquake events recorded on ~2, 389 seismic stations (Figure 2). This represents earthquakes with magnitude >5.5 spanning the period of 1989–2022. We select teleseismic earthquakes located at distances between 30 and 90° from the recording stations. This range is specifically chosen to exclude earthquakes that may be affected by diffraction effects in the core shadow zone (Hosseini et al., 2019), as well as non-planar and triplicated waves from the mantle transition zone (Stähler et al., 2012).

We apply several data cleaning and preconditioning procedures to ensure data quality. The seismograms are rotated from the geographic (Z, N, E) to the earthquake coordinate system: vertical (Z), radial (R), and transverse (T) orientation (Rondenay, 2009). We apply an automated quality selection criteria to obtain the best data. We select records with good signal-to-noise ratio (SNR), automatically rejecting all waveforms with SNR less than 2 (calculated with a signal window of 120 s and a noise window of 25 s around the predicted P-arrival time). We ensure consistent sampling rates across all waveforms for each station. This requires resampling the waveforms to the highest frequency for each station. Through these quality control measures, a total of 83,697 earthquake waveforms passed initial quality checks. This is a total of ~17% of the initial preprocessed data.

Figure 1. Compiled depths of US upper mantle discontinuities (UMD) highlighting the interference with crustal reverberation when imaging with P-to-S receiver functions (Ps-RFs). (a) A scatter plot of UMD depth (right y-axis) overlaid on the Ps delay time (left y-axis) of Moho multiples (red contours: pPmS and pSmS arrivals). This region delineates depth-range (and timing) of crustal interference with mantle conversions. The Ps-delay of mantle conversions and crustal reverberations are calculated using a continental-scale Moho model from Schmandt et al. (2015) and mantle velocities from Shen and Ritzwoller (2016). (b–d) Histogram of UMDs grouped by category. (e) Location where UMDs in (a) are observed anticipating locations where the Ps-RF imaging of UMDs are masked by crustal multiples (red). The symbols are same as in (a) and are from Abt et al. (2010), Krueger et al. (2021), Hopper and Fischer (2018); Hua et al. (2023), T. Liu and Shearer (2021), and Kind et al. (2020). The six-sided star with uncertainty bars in (a) represents an estimate based on the results reported in Kind et al. (2020), for which digital data was not available.

CARR AND OLUGBOJI 4 of 23

21699356, 2024, 5, Downloaded from https://agupubs.onlinelibrary.wiley.com/doi/10.1029/2024JB028781 by University Of Rochester, Wiley Online Library on [05/09/2024]. See the Terms and Condi

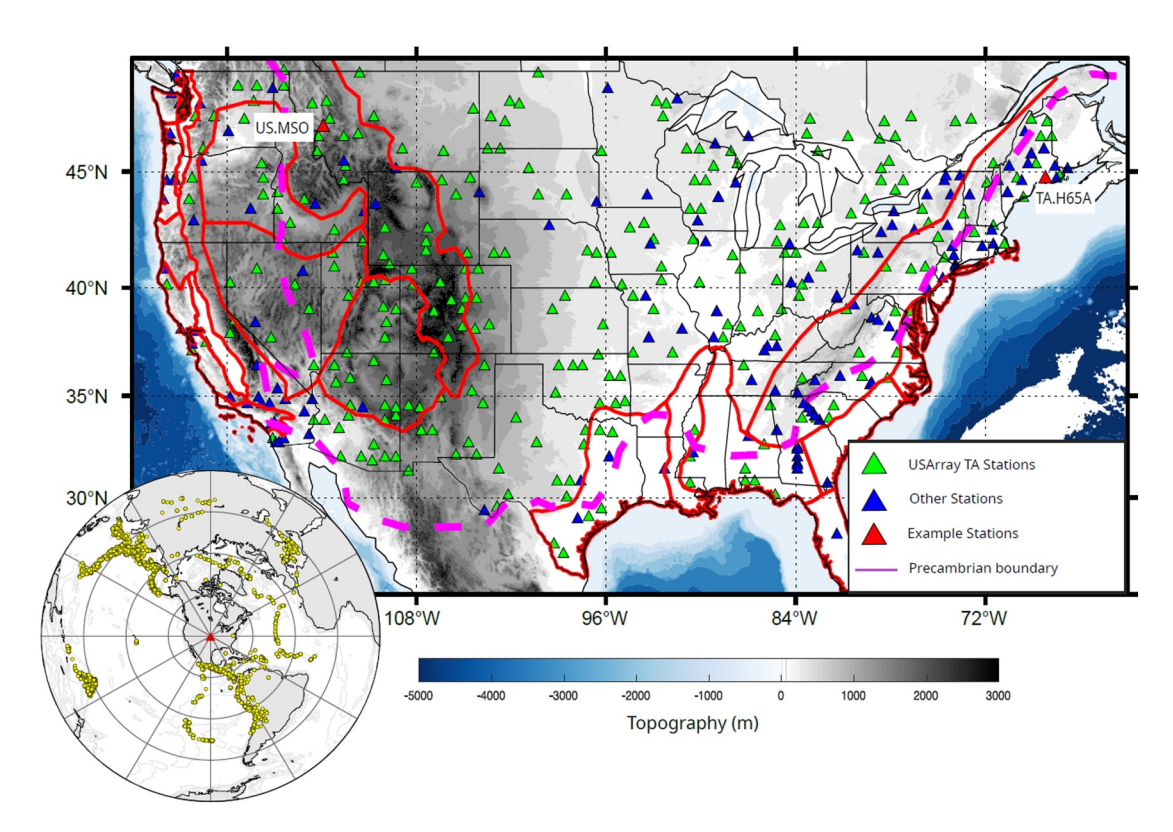


**Figure 2.** Distribution of 417 seismic stations used in this study. The inset shows the distribution of teleseismic earthquakes that are used. Red triangles mark the locations of the two example stations (TA.H65A, US.MSO) used in our analysis. A full description of all initial 2,389 stations and data statistics can be found in Figures S1 and S2 in Supporting Information S1. The outline of the Precambrian basement (pink) is obtained from Whitmeyer and Karlstrom (2007).

After the initial quality checks, we organize the seismograms recorded at each station into discrete slowness values. In a radially symmetric earth the body-waves propagating from the hypocenter to the station travel with a distinct ray parameter (slowness values) and sample the receiver-side structure with different arrival angles. Optimal slowness-sampling and epicentral distance coverage is required for stable CRISP-RF processing (Figure S2 in Supporting Information S1). This restriction reduces our station catalog from 2,389 to a final set of 417 stations (17.5% of total station inventory). This also culls the seismograms to a final selection of 20,460 of the best three-channel recordings. When compared to the discarded seismograms the final data set comprise the highest quality (SNR > 16) seismograms. Despite this strict data-selection criteria the final set of stations are widely distributed across the contiguous US ensuring a comprehensive coverage across different tectonic domains (Figure 2).

# 3. Methods

# 3.1. RFs at High-Frequency: Contaminated Radial Stacks

We image UMDs using high-frequency receiver functions. We analyze teleseismic P-waves for signature of conversion from seismic discontinuities beneath the stations (Langston, 1977). Radial Ps-RF traces are calculated with a cut-off frequency of 1.5 Hz using the extended-time multi-taper cross-correlation method (ETMT) (Helffrich, 2006). This approach extends the traditional cross-correlation receiver function technique (Park & Levin, 2016c) by applying multiple Slepian tapers to window the waveform data before spectral estimation and deconvolution. To improve the detection of late arriving low-magnitude sub-crustal mantle conversions, we employ a re-normalization procedure, where we implement a 6-s time-shift ( $\tau_s$ ) before applying the multiple Slepian tapers on the radial component traces (Equation 1a) (Helffrich, 2006; Park & Levin, 2016c; Shibutani et al., 2008). These steps preserve the amplitudes of late arriving phases and ensures that high-amplitude crustal phases do not overshadow the weaker and deeper sub-Moho conversions of interest. The time-shift is implemented in the frequency domain:

CARR AND OLUGBOJI 5 of 23

where  $U^r(\omega, p)$  is the Fourier-transformed radial seismogram and  $W_k$  are the Slepian tapers, and p is the horizontal slowness. The receiver functions are then computed by deconvolving the shifted radial seismogram from the vertical (both seismograms are tapered with  $W_k$ ):

$$\widetilde{\mathbf{D}}(\omega, p) = \begin{bmatrix} \sum_{\kappa=0}^{\kappa-1} \widetilde{U}_{\kappa}^{z}(\omega, p) * \widetilde{U}_{\kappa}^{r}(\omega, p) \\ \sum_{\kappa=0}^{\kappa-1} \widetilde{U}_{\kappa}^{z}(\omega, p) * \widetilde{U}_{\kappa}^{z}(\omega, p) + \zeta(\omega) \end{bmatrix}$$
(2)

We then stack the radial receiver functions in epicentral distance bins with one-degree spacing to enhance signal quality (Park & Levin, 2000, 2016b):

$$\mathbf{D}(\omega, p_s) = \left(\sum_{l=0}^{n_p} (1/\sigma_l^2)\right)^{-1} \left(\sum_{l=0}^{n_p} 1/\sigma_l^2 \widetilde{\mathbf{D}}(\omega, p_l)\right)$$
(3)

where  $p_s$  are the slowness bins,  $p_l$  are the individual slowness values in each bin, and  $\sigma_l^2$  are the frequency-dependent stacking weights derived from coherence (Park & Levin, 2000, 2016b). The frequency domain receiver functions are then transformed back to the time domain using the inverse Fourier transform

$$\mathbf{d}(t, p_s) = \mathcal{F}^{-1}[\mathbf{D}(\omega, p_s)] \tag{4}$$

where  $\mathcal{F}^{-1}$  is the inverse Fourier transform. The Ps-RF data is a 2-D matrix in which each row represents traces stacked into slowness bins. Each row is a distinct horizontal slowness and each column is a discrete-time sample. Each row is a single slowness stack centered in 1-degree bins with a 1-degree overlap between the bin centers. An example of a station with poor coverage (TA.H65A) and good coverage (US.MSO) is provided (Figure 3). For station H65A, a few slowness bins are empty because there are no earthquakes at these slownesses. Nevertheless, coherence across adjacent bins is good enough to identify the relevant conversions and multiples.

Since the crust-mantle boundary is often the most prominent discontinuity in the lithosphere, top-side reflections bouncing off the Moho (pPmS and pSmS) are visible in most of the stacked radial receiver functions (Figure 3). This presents a significant obstacle when interpreting converted waves from sub-crustal lithosphere discontinuities (100–200 km) arriving at ~10–20 s (Figures 1 and 3). The Moho multiples can be identified in the receiver function stacks by their characteristic time-distance (slowness) behavior. Moho multiples arriving early are from earthquakes located closer to the station and traveling with large horizontal slowness (Figure 3c). This is the opposite behavior for the Ps-converted waves that do not experience top-side reflections. These conversions arrive later for earthquakes located closer to the station (Ryberg & Weber, 2000; J. Shi et al., 2020). Depending on the station location, data quality, and depth to other discontinuities beneath a station, crustal multiples may not always be easily identified in the receiver function stacks. This makes it harder to interpret the final stacked receiver functions (Figures 3a, 3b, 3g, and 3h). For a clear and accurate interpretation of the Ps-RFs, it is crucial to distinguish crust-mantle top-side reflections from mantle conversion. Only when these multiply reflected waves have been properly filtered out can we confidently proceed with the interpretation for upper mantle layering.

# 3.2. Filtered RFs: CRISP-RF for Denoising

We briefly present our approach to removing top-side reflections and other non-coherent noise. This is the method called CRISP-RF (Olugboji, Zhang, et al., 2023). This method enhances the clarity of Ps-RFs allowing for a more accurate interpretation of sub-crustal mantle discontinuities. For a more detailed description, we refer the reader to (Olugboji, Zhang, et al., 2023). The technique involves three main steps: The initial step applies the sparse Radon transform to the Ps-RF data:

CARR AND OLUGBOJI 6 of 23

21699356, 2024, 5, Downloaded from https://agupubs.onlinelibrary.wiely.com/doi/10.1029/2024JB027871 by University Of Rochester, Wiley Online Library on [05/09/2024]. See the Terms and Conditions (https://onlinelibrary.wiely.com/doi/10.1029/2024JB027871 by University Of Rochester, Wiley Online Library on [05/09/2024]. See the Terms and Conditions (https://onlinelibrary.wiely.com/doi/10.1029/2024JB027871 by University Of Rochester, Wiley Online Library on [05/09/2024]. See the Terms and Conditions (https://onlinelibrary.wiely.com/doi/10.1029/2024JB027871 by University Of Rochester, Wiley Online Library on [05/09/2024]. See the Terms and Conditions (https://onlinelibrary.wiely.com/doi/10.1029/2024JB027871 by University Of Rochester, Wiley Online Library on [05/09/2024]. See the Terms and Conditions (https://onlinelibrary.wiely.com/doi/10.1029/2024JB027871 by University Of Rochester, Wiley Online Library on [05/09/2024]. See the Terms and Conditions (https://onlinelibrary.wiely.com/doi/10.1029/2024JB027871 by University Of Rochester, Wiley Online Library on [05/09/2024]. See the Terms and Conditions (https://onlinelibrary.wiely.com/doi/10.1029/2024JB027871 by University Of Rochester, Wiley Online Library on [05/09/2024]. See the Terms and Conditions (https://onlinelibrary.wiely.com/doi/10.1029/2024JB027871 by University Of Rochester, Wiley Online Library on [05/09/2024]. See the Terms and Conditions (https://onlinelibrary.wiely.com/doi/10.1029/2024JB027871 by University Of Rochester, Wiley Online Library on [05/09/2024]. See the Terms and Conditions (https://onlinelibrary.wiely.com/doi/10.1029/2024JB027871 by University Of Rochester, Wiley Online Library on [05/09/2024]. See the Terms and Conditions (https://onlinelibrary.wiely.com/doi/10.1029/2024JB027871 by University Of Rochester, Wiley Online Library on [05/09/2024]. See the Terms and Conditions (https://onlinelibrary.wiely.com/doi/10.1029/2024). See the Terms and Conditions (https://onlinelibrary.wiely.com/doi/10.1029/2024). See the Terms and Conditions (https

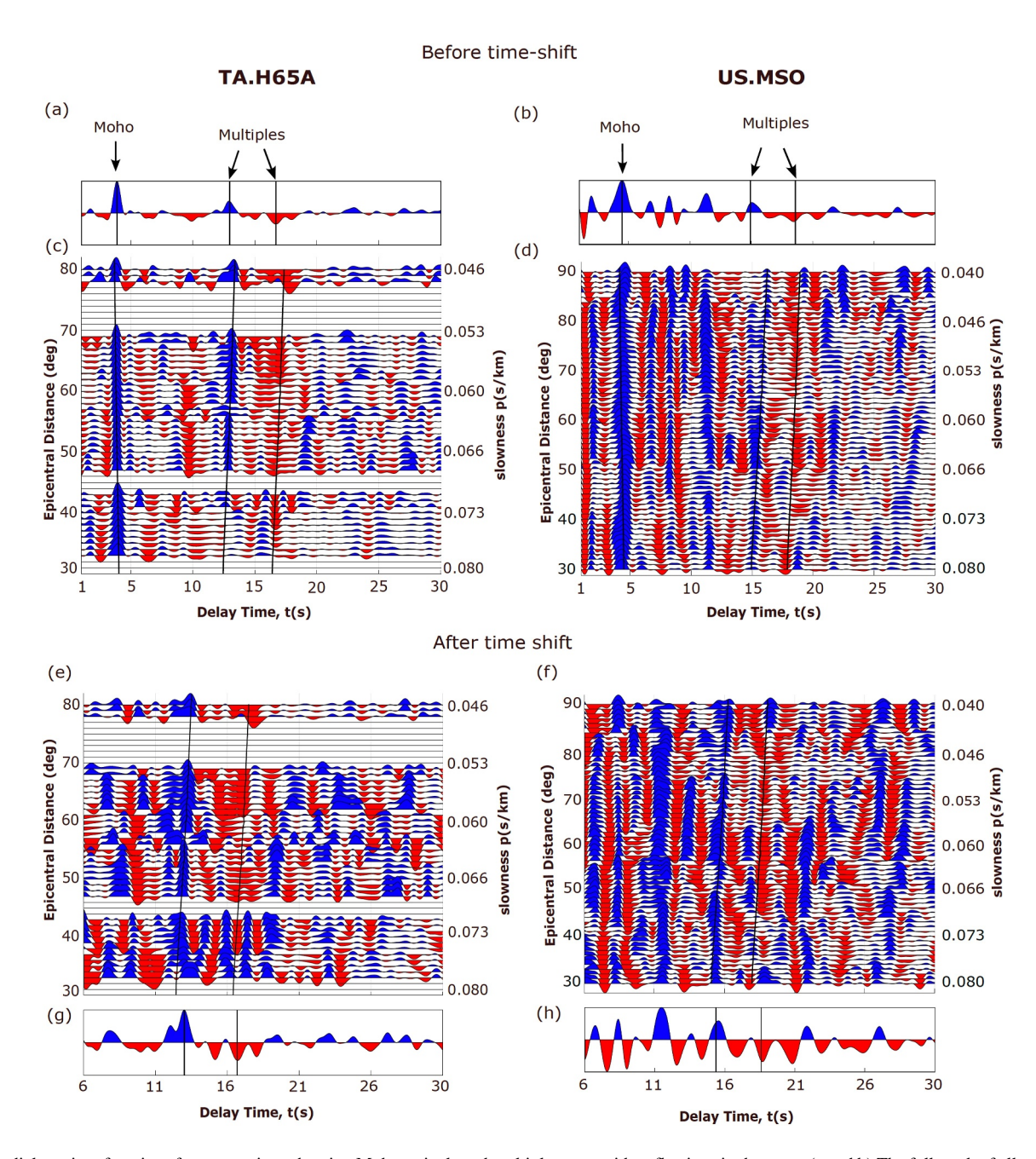


Figure 3. Radial receiver functions for two stations showing Moho arrivals and multiples—top-side reflections in the crust. (a and b) The full stack of all radial receiver functions for stations TA.H65A and US.MSO showing Moho and multiples. (c and d) The radial receiver functions for each station, sorted and stacked by station-earthquake distance in angular degrees. (e and f) Time-shifted radial receiver functions same as (c) and (d) but starting at 6 s (g and h) Full stack of the time-shifted receiver functions corresponding to (e) and (f). Blue and red shading indicate positive and negative amplitudes.

$$\mathfrak{R}_{sp}(\mathbf{d}) : \underset{\mathbf{m}}{\operatorname{argmin}} \left\{ \frac{1}{2} \| \mathcal{F}^{-1} \{ \mathbf{L} \mathcal{F} \{ \mathbf{m} \} \} - \mathbf{d} \|_{2}^{2} + \lambda \psi(\mathbf{m}) \right\}$$
 (5)

where  $\Re_{sp}(\mathbf{d})$  maps the Ps-RF data  $\mathbf{d}$  to the Radon model  $\mathbf{m}$ . The transform can be viewed as finding a predictive Radon model,  $\mathbf{m}$ , using the forward operator  $\mathbf{A}$  and subject to regularization  $\psi(\mathbf{m})$  (recasting as  $\mathbf{d} = \mathbf{A}\mathbf{m}$ ). Therefore the transform is an optimization problem to find  $\mathbf{m}$  using a sparsity-enforcing regularization:  $\ell_1$ -norm  $\psi(\mathbf{m}) = \|\mathbf{m}\|_1$  (Equation 5). This optimization is solved using the SRTFISTA algorithm: a fast iterative shrinkage-thresholding approach that promotes the sparsity of the Ps-RFs in both the time and frequency domains (forward

CARR AND OLUGBOJI 7 of 23

21699356, 2024, 5, Downloaded from https://agupubs.onlinelibrary.wiley.com/doi/10.1029/2024JB028781 by University Of Rochester, Wiley Online Library on [05/09/2024]. See the Terms and Conditions (https://acade.com/ac

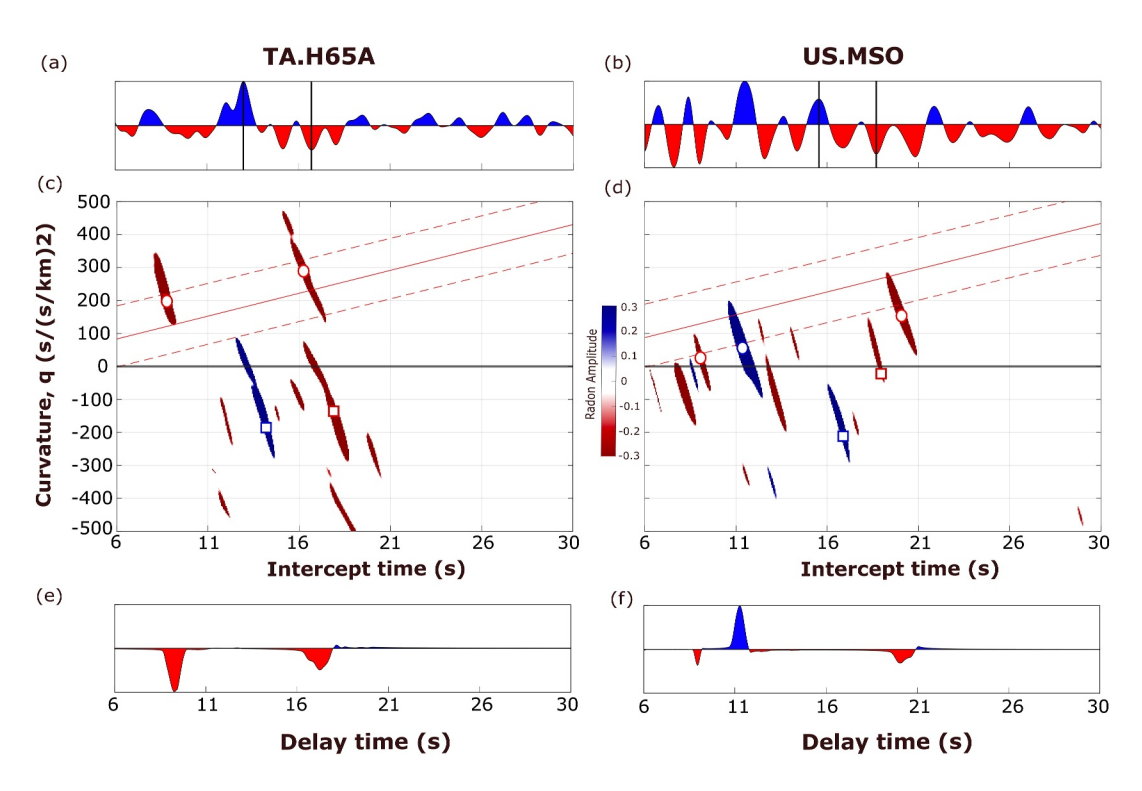


Figure 4. Clean Receiver-function Imaging using Sparse Radon Filters denoising steps for filtering receiver functions obtained from stations TA.H65A and US.MSO. (a and b) Time-shifted unfiltered receiver function stacks, with predicted Moho reverberation times indicated by black lines. (c and d) Radon model (after applying step 1) showing direct mantle conversions along the positive curvature axis (circles), and multiples in the negative curvature (squares). The masking filter are the red lines—they retain all arivals between the dashed lines (step 2). (e and f) The final filtered P-to-S receiver functions after transforming the filtered Radon model to data domain (step 3). The top-side reflections in the crust have been removed leaving only the direct conversions.

and inverse Fourier operators:  $\mathbf{A} = \mathcal{F}^{-1}\mathbf{L}\mathcal{F}$ ) and yields a cleaner representation of the Ps-RF data (Beck & Teboulle, 2009; Gong et al., 2016). Here,  $\mathbf{L}$ , is a frequency-domain projection matrix that maps the Ps-RF arrivals in  $\mathbf{d}$  from the time-slowness data-space to the Radon model,  $\mathbf{m}$ , which is now in the intercept-time-curvature model-space. Top-side reflections are mapped into the negative curvature while direct conversions show up in the positive curvature (Figures 4c and 4d).

The second step applies a selective masking filter,  $\mathbf{K}$ , to the Radon model  $\mathbf{m}$ . The filter is designed to extract only direct mantle conversions by removing contributions representing top-side reflections (red dashed lines in Figures 4c and 4d). By setting the amplitudes with negative curvatures (squares in Figures 4c and 4d) to zero and preserving those with positive curvatures (circles in Figures 4c and 4d), the masking filter retains only Ps-conversions from the upper mantle. The third and final step transforms the now filtered Radon model back to the data-space using the adjoint Radon transform  $\mathfrak{R}_{sp}^+$ . This is the required filtered Ps-RF data  $\widetilde{\mathbf{d}}$  free of unwanted reflections and incoherent noise (Figures 4e and 4f):

$$\mathbf{d} \xrightarrow{\mathfrak{R}_{sp}} \mathbf{m} \xrightarrow{\mathbf{K}} \mathbf{m} \mathbf{K} \xrightarrow{\mathfrak{R}_{sp}^{\mathfrak{R}_{sp}^{+}}} \widetilde{\mathbf{d}}$$

$$(6)$$

A comparison between the original and CRISP-RF processed Ps-RF stacks for our two example stations shows that the CRISP-RF technique has successfully isolated the mantle-converted phases by attenuating crustal multiples and noise (compare Figures 4a and 4b to Figures 4e and 4f). This is evident in the filtered stacks, where mantle conversions are easily and unambiguously identified.

CARR AND OLUGBOJI 8 of 23

21699356, 2024, 5, Downloaded from https://agupubs.onlinelibrary.wiley.com/doi/10.1029/2024JB028781 by University Of Rochester, Wiley Online Library on [05/09/2024]. See the Terms and Conditions (https://

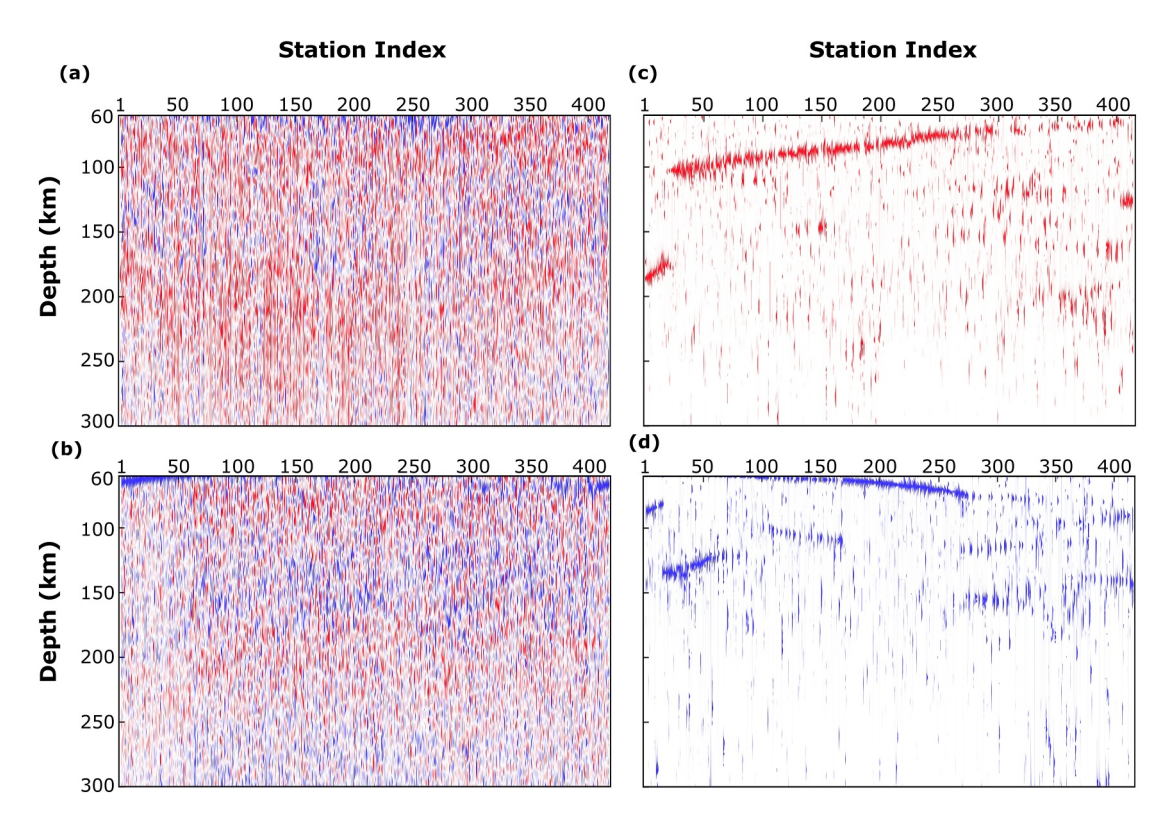


**Figure 5.** Enhanced pattern recognition of upper mantle discontinuities through polarity-based filtering and sequencing of P-to-S receiver function (Ps-RF) traces. (a) Single-station radial Ps-RF stacks without Clean Receiver-function Imaging using Sparse Radon Filters (CRISP-RF) processing illustrating minimal interpretive content (b) Single-station radial Ps-RF traces, same as in (a), but processed through the sequencer algorithm. The image is still hard to interpret due to the presence of multi-mode scattering in a heterogeneous crust (c) Negatively filtered and sequenced Ps-RF traces (d) positively filtered and sequenced Ps-RF traces. The CRISP-RF filtered traces in (c) and (d) show clear and coherent arrivals.

### 3.3. Machine Learning (Sequencing and Clustering) on Filtered RFs

Since our aim is to produce a detailed map of coherent scattering across discontinuities located in the upper mantle, we employ a two-tiered machine-learning approach to find repeatable patterns in the receiver function signature of upper mantle conversions across all our 417 stations. This approach integrates the Sequencer algorithm (Baron & Ménard, 2020) with hierarchical clustering, each serving a distinct but complementary role in uncovering patterns in our denoised Ps-RFs. The sequencer algorithm is necessary for sorting the CRISP-RF filtered receiver functions before applying the correlation-based hierarchical clustering algorithm. The Sequencer algorithm is an unsupervised machine learning tool that reveals hidden sequential structures often obscured within complex multivariate data sets (Baron & Ménard, 2020). It leverages a variety of distance metrics to systematically reorder data sets based on similarity. It has shown promise in sequencing earthquake waveforms to discern spatial patterns in lower mantle scattering (Kim et al., 2020), the analysis of seismic noise to detect temporally coherent signals (Fang, 2024), and classification of seismic velocities for guiding the discovery of tectonic influences on crustal architecture (Olugboji, Xue, et al., 2023). In our application of the sequencer algorithm, the data objects to be sequenced are the single-station Ps-RF stacks obtained before or after CRISP-RF processing (vertical lines in the images of Figure 5).

First, we apply the Sequencer to the unfiltered single-station receiver function stacks (Figure 5a). The performance is very poor (Figure 5b). A slight improvement in the detection of positive amplitude arrivals can be seen at  $\sim$ 60 and  $\sim$ 100 km but not much information is gained from ordering the unfiltered data. This is probably due to the complex mixed-mode scattering within the highly heterogeneous crust across the US. As a result, it is hard for the sequencer algorithm to find interpretable patterns within the data. On the other hand, when we separate CRISP-RF filtered receiver function into two subsets: a set containing only negative amplitudes, and another with only positive amplitudes, the algorithm performed much better. This is possible because we have filtered out the top-side reflections in the crust as well as other incoherent noise. The additional simplification using polarity-

CARR AND OLUGBOJI 9 of 23

dependent filtering also helps considerably (Figures 5c and 5d). We use an appropriate measure of dissimilarity (Kullback-Leibler (KL) divergence) and a scale (16) to find the most optimal ordering of each of the two data subsets. The (KL) divergence measures the dissimilarity between two data objects using an estimate of relative entropy, while the scale subdivides the data vectors into smaller contiguous sub-units in order to scan for patterns at longer wavelengths (Baron & Menard, 2020). The importance of filtering and de-noising with CRISP-RF before sequencing is another strong argument for why we are able to improve our detection of upper mantle layering using Ps-RFs that are clearly overprinted by a highly scattered wave-field within the continental crust (Figures 1 and 5a).

After sequencing the filtered Ps-RFs, we apply a hierarchical clustering algorithm to associate the seismic stations into groups. Hierarchical clustering starts by measuring pair-wise cross-correlation across all the filtered Ps-RFs. This measure of similarity is then used to create binary clusters in a hierarchical manner. For example, a third object is merged into the binary cluster containing the two objects and so on until all objects are included in a final master cluster. This cluster tree (dendogram) is a visual representation of linkages (similarity metrics) between the Ps-RFs. The most consistent Ps-RFs have linkages that are short while the dissimilar ones have longer linkages. We use the dendogram to inform initial cluster groupings by selecting a linkage threshold (Figures S3 and S4 in Supporting Information S1). This initial grouping is refined through the merging of certain cluster pairs based on depth coherence (see example P2a and P2b of Figure S3 in Supporting Information S1). This refinement produces four final clusters: one set for the positively filtered Ps-RFs and another set for the negatively filtered Ps-RFs (Figures 6 and 7). Each cluster represents an collection of single-station polarity-filtered Ps-RFs whose traces exhibit the highest degree of similarity, thereby reflecting the signature of scattering from coherent upper mantle stratification.

### 4. Results

Unsupervised machine learning, applied to Ps-RF traces that have been filtered based on polarity, offers a window into upper mantle structure beneath the contiguous US. Based on our analysis we observe a more complicated stratification of upper mantle structure. Beneath each station, three types of UMDs are observed, classified based on depth: (a) intra-lithospheric discontinuities (velocity reduction and increase), (b) transitional discontinuities (velocity reduction) and (c) sub-lithospheric discontinuities (velocity increase). This observation presents a departure from the simple view of a single uniform and ubiquitous mid-lithosphere discontinuity expressed as a rapid velocity decrease. Note that the relationship of the discontinuity depth to location within, across or beneath the lithosphere is only straightforward for stable continental lithosphere. In more tectonically active regions of the US, the association of the cluster depths to terms like lithosphere is not straightforward. That said, this detailed perspective on upper mantle layering may reflect changes in composition, metasomatism, phase change, or rheology.

### 4.1. Transitional and Intra-Lithosphere Discontinuities: Velocity Decrease

The most striking results is the detection of phases with negative polarity visible across all the stations and within depth internal to the lithosphere (<200 km) and at a depth that marks a transition from the lithosphere to asthenosphere (>200 km). These phases with negative polarity on the filtered Ps-RF traces indicate discontinuities marked by a velocity decrease. After coherence-based clustering of these negative discontinuities, we observe four distinct station groupings: N1–N4 (Figure 6 and Figure S5 in Supporting Information S1). The group index is sorted based on the total number of stations and depth of each group's representative centroid (average Ps-RF trace in each cluster).

The first and largest cluster, N1, (45%—189 of 417 stations) is the one with a pronounced Ps-RF arrival at a depth between 60 and 100 km, that is, spanning a depth of ~40 km (Figures 6a and 6b and Figure S5a in Supporting Information S1). This intra-lithosphere discontinuity is within the depth range traditionally associated with the mid-lithosphere discontinuity reported in previous studies (see Figure 1b) (Abt et al., 2010; Hopper & Fischer, 2018; Hua et al., 2023; Krueger et al., 2021; T. Liu & Shearer, 2021). Our independent confirmation of this discontinuity using a slightly different approach, Filtered and Sequenced Ps-RFs instead of Sp-RFs, provides extra validation that this discontinuity is real and not an artifact of deconvolution.

The second largest cluster, N2, (24%—101 of 417 stations) represents all stations with slightly deeper Ps arrivals compared to N1: 100–135 km. This discontinuity is more depth-confined. Half of the stations see the

CARR AND OLUGBOJI 10 of 23

onlinelibrary.wiley.com/doi/10.1029/2024JB028781 by University Of Rochester, Wiley Online Library on [05/09/2024]. See the Terms and Conditions (https://onlinelibrary

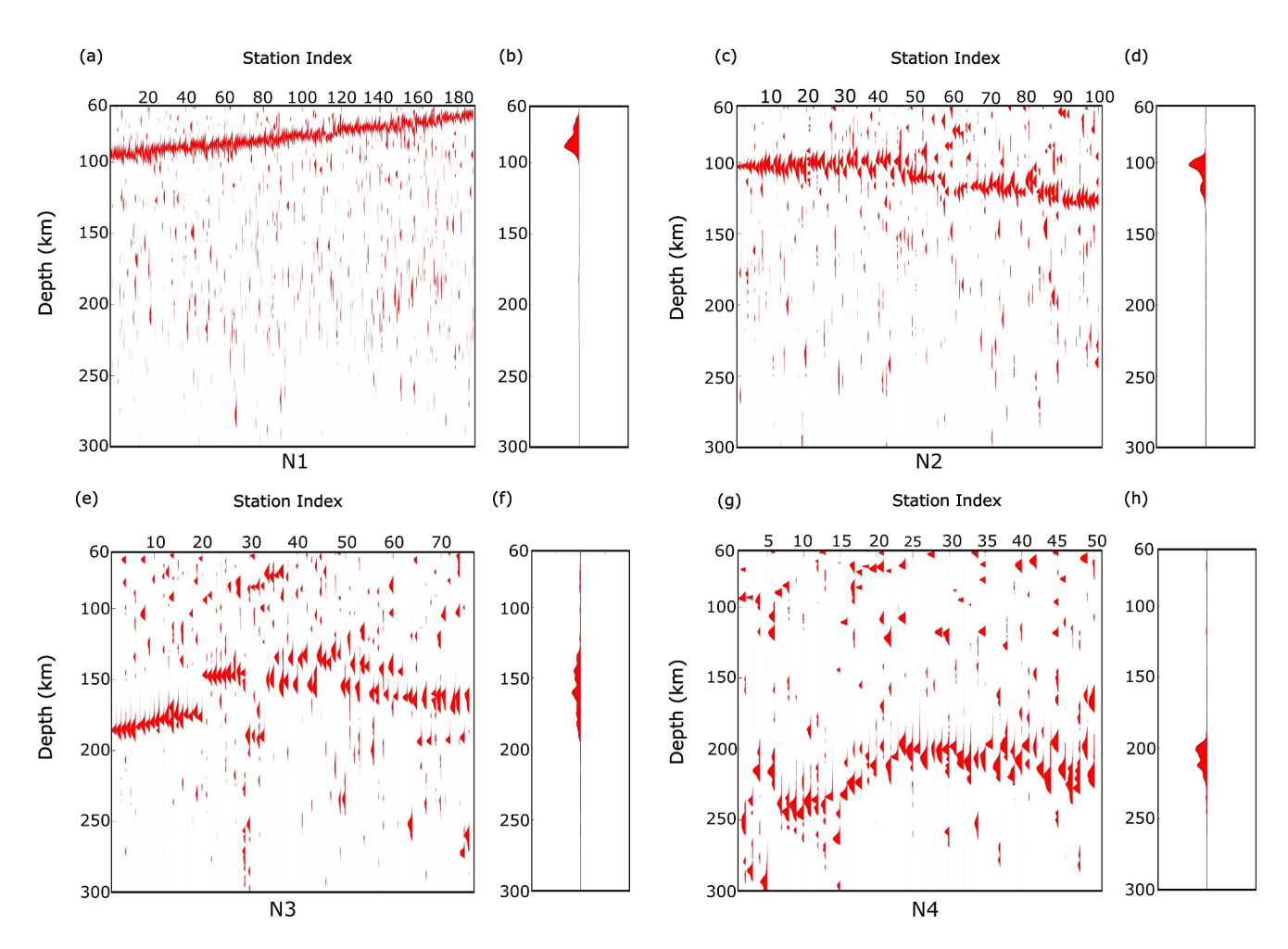


**Figure 6.** Stations with upper mantle discontinuities marked by a velocity decrease and grouped by the hierarchical clustering of filtered and sequenced P-to-S receiver functions (Ps-RFs) (a) Shallow intra-lithosphere discontinuity (60–100 km) sorted from the deepest to shallowest station with the depth spanning 40-km. This discontinuity is similar to the previously identified mid-lithospheric discontinuities in Figure 1b. (b) Semblance-weighted stacks of the individual single-station filtered Ps-RFs (c) A relatively consistent and shallow intra-lithospheric discontinuity (100 and 135 km) (d) Semblance-weighted stack, same as in (b), showing the average Ps-RF signature across all stations in the cluster. (e) A transitional discontinuity (150–190 km) located at a depth consistent with the bottom of a thermal boundary layer. (f) The semblance weighted stack showing a more diffuse trace due to larger variance across stations in the cluster (g) a transitional discontinuity (200–250 km) located at a depth consistent with the transition from a conductive to adiabatic thermal gradient in a cold cratonic lithosphere. (h) The semblance weighted stack, is impulsive (~200 km) when the within-cluster variance is small and suggests that the sporadic negative amplitudes (~100 km) are not spatially coherent. A full statistic of the depths can be found in Figure S5 of the Supporting Information S1.

discontinuity at a depth of 100 km and another half 35 km deeper at ~135 km (Figures 6c and 6d and Figure S5b in Supporting Information S1). Compared to its shallower counterpart in N1 (Figure 6a), the deeper reflector lacks a substantial depth variability and hints at a relatively consistent physical process across this limited depth range. While sporadic detections of such a relatively deeper intra-lithosphere discontinuity have previously been reported especially within the Achaean and Proterozoic terrains of central and eastern US, (Hua et al., 2023; T. Liu & Shearer, 2021), the consistency of this seismic signal in a quarter of our stations implies a more widespread occurrence.

The third cluster, N3, (18%—77 of 417 stations) represents stations with the deepest intra-lithosphere reflectors located at a depth range from  $\sim$ 150 to  $\sim$ 190 km (Figures 6e and 6f and Figure S5c in Supporting Information S1). Coherent signals in this depth range coincide with the lowermost region of the thermal boundary layer within cratonic lithosphere (Kind et al., 2020) and may mark the transitional zone where a non-mobile lithosphere transitions to a convecting upper mantle asthenosphere. Although these groups of stations are consistent in having deeper discontinuities, we observe a few stations with shallower discontinuities which are not located at a

CARR AND OLUGBOJI 11 of 23

21699356, 2024, 5, Downloaded from https://agupubs.onlinelibrary.wiley.com/doi/10.1029/2024JB028781 by University Of Rochester, Wiley Online Library on [05/09/2024]. See the Terms and Conditions (https://onlinelib

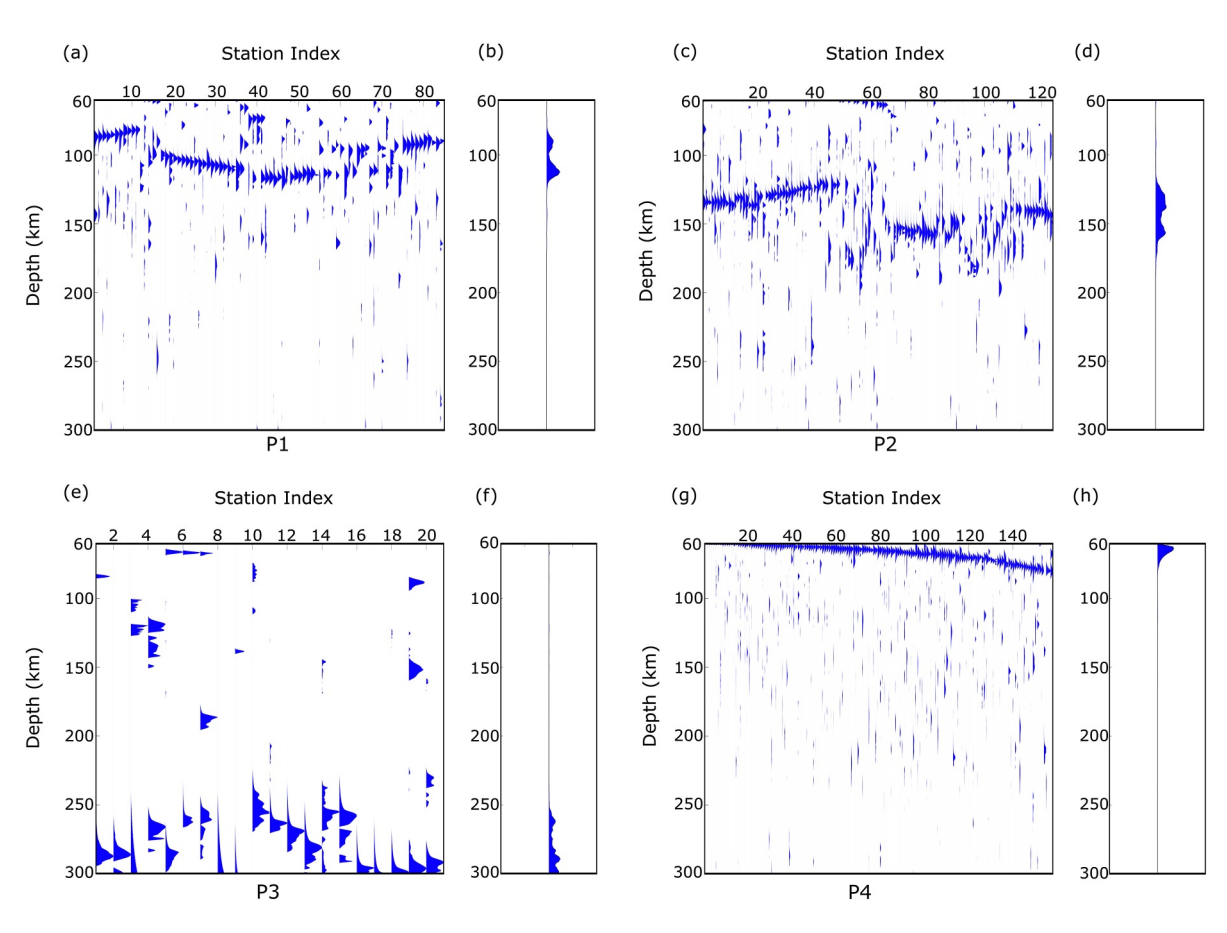


Figure 7. Similar to Figure 6 but for upper mantle discontinuities marked by a velocity increase. (a) P1: intra-lithosphere discontinuity depth of  $\sim$ 80–120 km (c) P2: intra-lithosphere discontinuity at a depth of  $\sim$ 120–180 km (e) P3: sub-lithosphere discontinuity at a depth of  $\sim$ 250–300 km (g) P4: Null detection potentially caused by a sub-crustal transitional layer. (b, d, f, h) Semblance-weighted stacks summarizing mean P-to-S receiver function signal for P1–P4. A full statistic of the depths can be found in Figure S6 in Supporting Information S1. The spatial clustering can be found in Figure S8 in Supporting Information S1.

consistent depth. This complicated pattern reduces the overall correlation value across the entire group. as indicated by the smearing in the final cluster average (Figure 6f).

The fourth and final cluster, N4, (12%—50 of 417 stations) represents stations that detect a discontinuity that is very clearly transitional between lithosphere and asthenosphere (Figure 6g). This is seen as a clear negative arrival on the Ps-RFs at a depth consistently between 200 and 260 km (Figure 6g). This depth range coincides with the expected base of thick depleted rigid mantle lithosphere underneath cratons (Kind et al., 2020). As such, this cluster of stations reflects a deeper lithosphere-asthenosphere transition, and may be a strong signature of an impedance contrast between the rigid lithospheric mantle and the weaker asthenospheric mantle. Stations that belong to this group, and in part N3, are consistent with upper mantle stratification previously reported by (Kind et al., 2020) in the central and eastern US referred to as the cratonic LAB. Here, our results show that these stations are mostly located in the Eastern US, for N4, with some stations in the western US for N3 (see Figures S7c and S7d in Supporting Information S1)

### 4.2. Intra and Sub-Lithosphere Discontinuities: Velocity Increase

In addition to UMDs marked by a velocity decrease, we present results for discontinuities marked by a velocity increase. The Ps-RF signature of a velocity increase is a positive amplitude on the filtered Ps-RF traces. With the Ps-RFs filtered for positive amplitudes (Figure 5d) and processing through the hierarchical clustering algorithm, we observe two main types of UMDs marked by a velocity increase: (a) intra-lithospheric and (b) sublithospheric. The first cluster, P1, represents 22% of the stations with the shallowest intra-lithospheric discontinuity between  $\sim$ 80 to  $\sim$ 120 km (Figure 7a). This discrete jump in velocities is at a depth range overlapping with the intra-lithospheric discontinuities marked by a velocity decrease in clusters N1 and N2 (Figures 6a and 6c).

CARR AND OLUGBOJI 12 of 23

Slightly deeper (by  $\sim$ 40 km) is a second cluster, P2, of 32% of the stations located above a velocity increase located between  $\sim$ 120 to  $\sim$ 180 km (Figure 7c). This intra-lithosphere discontinuity coincides with the previously reported PVG-150 km discontinuity (PVG-150) which has been hypothesized to be the base of a low velocity zone within the asthenosphere (Hua et al., 2023). When paired with the intra-lithosphere reflectors marked by a velocity decrease, this discontinuity reveals a potentially stratified lithospheric mantle in some regions (Figure S8 in Supporting Information S1). Detection of such a top and bottom interfaces is only separable using these two-tier filtering and clustering approach.

A third cluster, P3, unlike the other two, indicates the detection of an elusive sub-lithosphere discontinuity at  $\sim$ 250–300 km (Figure 6e). Only a few stations ( $\sim$ 5%) show clear Ps-RF arrivals at these depths (Figure 7e). This observation is consistent with the reported depth of the previously detected X-discontinuities (Pugh et al., 2021, 2023), which has remained elusive in prior studies of upper mantle layering across the contiguous US. The final and largest cluster, P4, is a null detection for lithosphere or sub-lithosphere discontinuities with a velocity increase. This is  $\sim$ 41% of the station population. In this cluster, the positive amplitudes observed at depths  $\sim$ 60 km (Figures 7g and 7h) are most likely a signature of thickened crust or terrain sutures expressed in data as a double Moho, a dipping layer or an anisotropic boundary (Levin et al., 2023) (see Figures S10 and S11 in Supporting Information S1). In most cases, these stations are spatially correlated with N1–N3 (compare Figure 10b with Figure S8d in Supporting Information S1). These structures may be associated with complexes formed during the extended Paleozoic assembly of the North American continent.

### 4.3. Spatial Clustering of Stations and Ps-RF Centroids

Up until now, we've grouped our filtered Ps-RF results by looking at the data-similarity without any concern for geology or tectonics. Now, we examine how the stations belonging to each cluster are distributed in space. We do this by color-coding each station by the cluster index it belongs to using a color-coding scheme that interpolates stations into a 1-degree bin (Figures 8b and 8d). The mantle-discontinuity structure (velocity increase or decrease) beneath each station is then approximated by the representative Ps-RF centroid for each group. The centroid is a semblance-weighted stack for all the polarity-filtered Ps-RFs for all the stations in the group. This summarizes the data variance in each group to a set of archetype receiver function reflecting the depth-dependent discontinuity structure across the US (Figures 8a and 8c). This spatial analysis of the station clustering reveals a striking diversity in upper mantle layering. It shows a mosaic of negative and positive seismic structures distributed in a largely stochastic fashion (Figures 8b and 8d). We observe that no single boundary or transition predominates continent-wide. Instead, a spectrum of seismic discontinuities emerges, segmented across variable depths. This random distribution does not conform to simple geographical or tectonic boundaries.

Despite this broad characterization, we observe that the most prevalent mantle discontinuity is the *intralithospheric discontinuity with a velocity decrease* which is observed at  $\sim$ 70% of our stations (N1 + N2). The semblance-weighted mean stacks reflect a discontinuity at  $\sim$ 100 km for both clusters. In the first cluster, N1, the precursory arrival reflects the systematic depth variation across the individual Ps-RFs and for the second cluster, N2, the post-cursor arrival represents the slight depth offset for half of the station. Regardless these two clusters represent most of the data-variance for a negative-amplitude Ps-RFs. The filtered Ps-RF traces from these stations show a high correlation coefficient which is visually confirmed in the data grouping (compare Figures 6a and 6c). Beneath 18.22% of our stations, we observe that the deepest intra-lithosphere discontinuity, N3 is less coherent (Figure 8a). The last group of stations, only 12%, provide evidence for a discontinuity that is transitional between the lithosphere and asthenosphere—N4—with a representative Ps-RF that is  $\sim$ 200 km (Figure 8a). The interstation coherence for this group is slightly better than that of N2 but less than N1 and N2. The stations detecting this deeper transitional discontinuity are more prevalent in the stable continental lithosphere of the eastern US (Figure S7d in Supporting Information S1).

For the upper mantle marked by a velocity increase, we observe only intra-lithospheric and sub-lithospheric discontinuities. We do not observe velocity increases at depths transitional between lithosphere and asthenosphere ( $\sim$ 200 km). While the stations distribution shows no clear separation by geology or tectonics, we observe that the largest cluster (41%), P4, is a null detection for UMDs (Figures 7h and 8d). This means that intra-lithosphere discontinuities (P1 + P2 = 53%) are unlikely than the counterpart velocity decrease (N1 + N2 = 70%). The discontinuity structure beneath stations in cluster P1 is slightly shallower ( $\sim$ 100  $\pm$  20 km), more self-similar (higher correlation) than those in P2 ( $\sim$ 150  $\pm$  30 km), which are deeper. Unlike the intra-

CARR AND OLUGBOJI 13 of 23

21699356, 2024, 5, Downloaded from https://agupubs.onlinelibrary.wiey.com/doi/10.1029/2024JB028781 by University Of Rochester, Wiley Online Library on [05/09/2024]. See the Terms and Conditions (https://onlinelibrary.wiley.

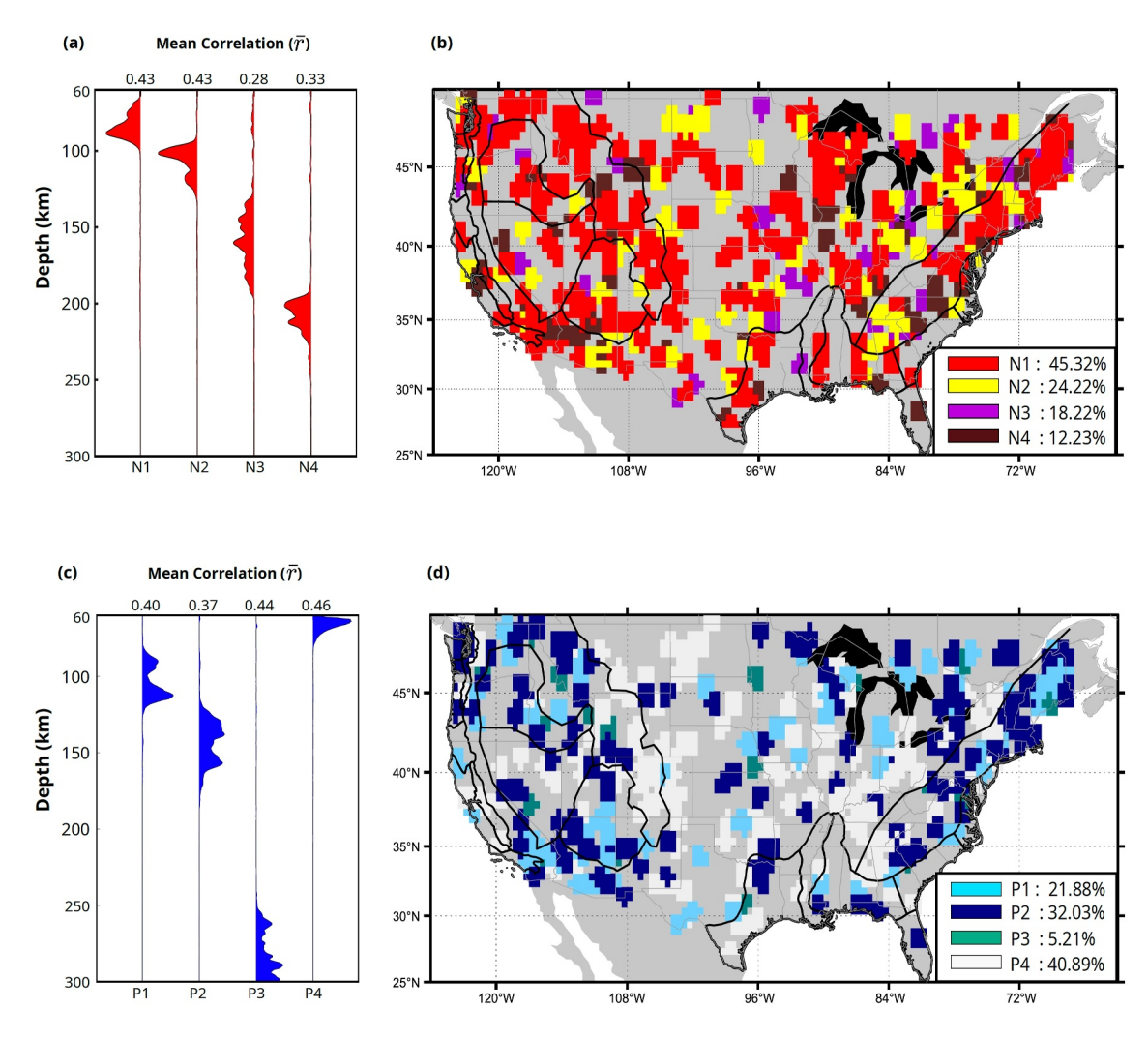


**Figure 8.** Station location, cluster index, centroid, and statistics for each P-to-S receiver function (Ps-RF) filtered by polarity. (a) Semblance-weighted stacks for negative Ps-RF traces (N1–N4) representing discontinuities within and across the lithosphere (b) Location of stations (and counts) belonging to cluster N1–N4 (c) Semblance-weighted stacks for positive Ps-RF traces (P1–P3) representing discontinuities within and beneath the lithosphere. P4 represents null detections unrelated to upper mantle structure (d) Location of stations (and counts) belonging to cluster P1–P4.

lithosphere discontinuities, the detection of sub-lithospheric discontinuities are rare. Only 5.21% of stations belong to cluster 3 (Figure 7e). The depth range is confined to ( $\sim$ 270  $\pm$  30 km). The detection of UMDs with variable depth and spatial distribution reflects a complexity inconsistent with a simple view of a laterally continuous boundary. This complexity underscores their detection by higher resolution Ps-RFs after appropriate filtering and sorting.

# 4.4. Synthesis: Architecture of Upper Mantle Stratification

The analysis of polarity-filtered single-station Ps-RF traces resulted in their classification based on the upper mantle structure beneath the station. When each station was processed through the CRISP-RF filter and sorted into an exclusive group: N1–N4 or P1–P4 based on similarity to other stations, we were able to distinguish depth and type of the discontinuity (e.g., shallow, deep, velocity decrease or intra-lithospheric). However, it is important to note that each station can belong to either an "N-cluster", a "P-cluster", or both. Therefore looking beneath each station and identifying the "N-discontinuity" or "P-discontinuity" structure leads to a view of upper mantle architecture across the US. The first class is the *intra-lithosphere discontinuities without a discernible base* (green circles in Figure 9). These are stations whose Ps-RFs belong to the relatively shallow "N-clusters" (N1–N3) but do not indicate a deeper discontinuity marked by a velocity increase and so do not have a "P-cluster" signature (do not belong to P1–P3). Crucially, these stations are coincident with the P4-cluster (null detection) (see Figure S8d

CARR AND OLUGBOJI 14 of 23

com/doi/10.1029/2024JB028781 by University Of Rochester, Wiley Online Library on [05/09/2024]. See the Terms

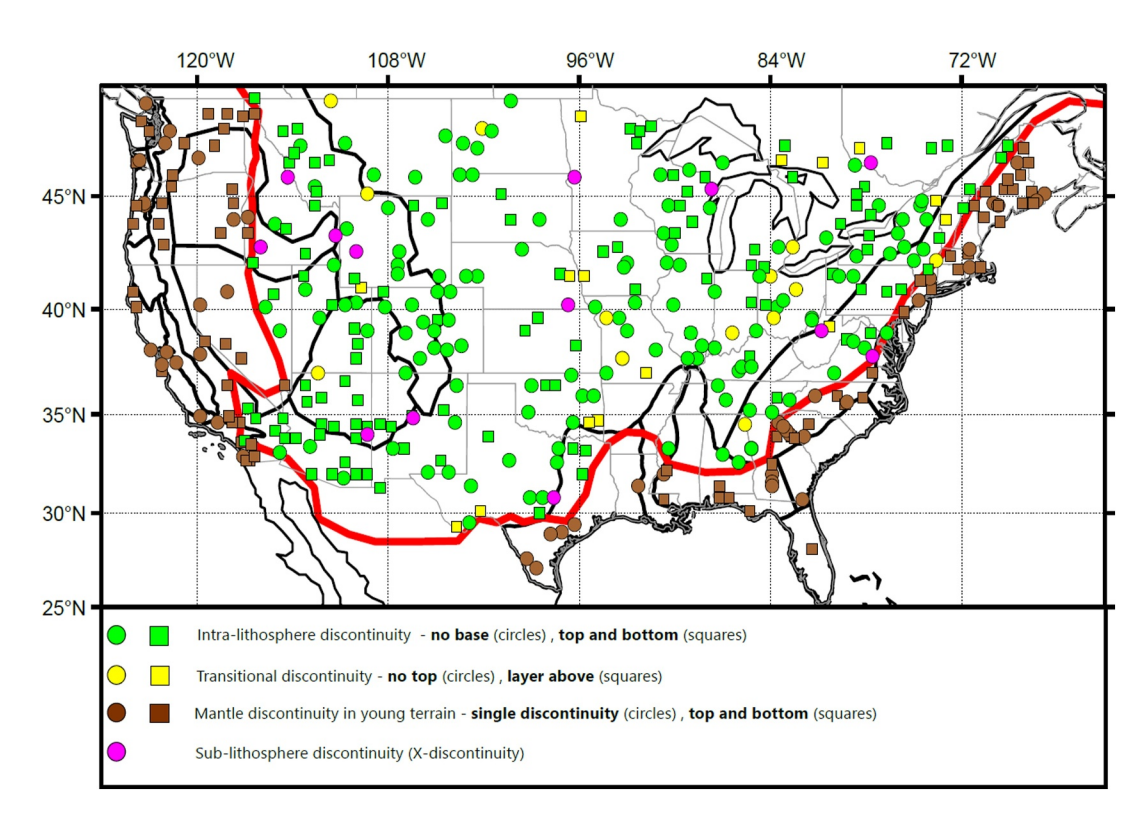


**Figure 9.** Upper mantle stratification beneath the US. Intra-lithosphere discontinuities—green. Transitional discontinuities—yellow. Upper mantle discontinuity in young terrain—brown. Sub-lithosphere discontinuities—magenta. Single discontinuities are represented by circles and paired discontinuities are represented by squares.

in Supporting Information S1), where deep crustal reflectors and no positive intra-lithosphere discontinuities are observed. The absence of a velocity increase below the velocity decrease indicates that this is a strict discontinuity rather than a layering with a discernible top and bottom base. This type of upper mantle structure is widespread (35% of recording stations) suggesting a ubiquitous feature of the lithosphere.

A second class of intra-lithosphere discontinuities is those that show up as a paired discontinuity. This type of upper mantle stratification is as prevalent as the previous type (32% of recording sites). This upper mantle architecture is observed for stations that belong to both an "N-cluster" (N1–N3) and a "P-cluster" (P1 and P2) cluster. Therefore beneath these stations, the mantle has both an upper and lower impedance contrast as you cross through an intra-lithosphere layer (green squares in Figure 9). It is important to note that two potential stratifications can arise in this conjunction of "N-cluster" and "P-cluster" discontinuities: (a) a layer bounded by a velocity decrease on top and a velocity increase below, and (b) the reverse, a layer bounded by a velocity increase on top and a velocity decrease below (details in Figure 10a). The latter is a special case of mid-lithosphere stratification that has not previously been resolved.

The last two classes of upper mantle stratification are: *transitional discontinuities* across the lithosphere and asthenosphere (yellow symbols in Figure 9) and *sub-lithosphere discontinuities*. Both types are not widespread —only 8% of our stations show the detection of transitional discontinuities within the upper mantle. The transitional discontinuities are either single discontinuities (circles in Figure 9: "N4" or deep "N3" clusters) or paired with a top-boundary that is a velocity increase (squares in Figure 9: "P1 or P2"). Lastly, sporadic detection of sub-lithosphere discontinuities (4.7% of stations) belonging to the "P3-cluster" constitutes the final class of upper mantle stratification (magenta-colored stations in Figure 9). These are velocity increases confined to a depth of  $\sim 250 \pm 300$  km. As pointed out earlier, we choose to use the more generic term "mantle discontinuities" for single and paired discontinuities observed in young terrain (20% of recording stations) (brown symbols in Figure 9). Previous authors may refer to these boundaries as transitional (e.g., the LAB). We note that in some cases, for example, on the edges of Precambrian terrain or within the Snake River Plain, which has been argued to have experienced lithosphere delamination (Y.-N. Shi & Morgan, 2022), our classification should be interpreted with

CARR AND OLUGBOJI 15 of 23

21699356, 2024, 5, Downbaded from https://agupubs.onlinelibrary.wiley.com/doi/10.1029/2024JB028781 by University Of Rochester, Wiley Online Library on (05/09/2024). See the Terms and Conditions (https://onlinelibrary.wiley

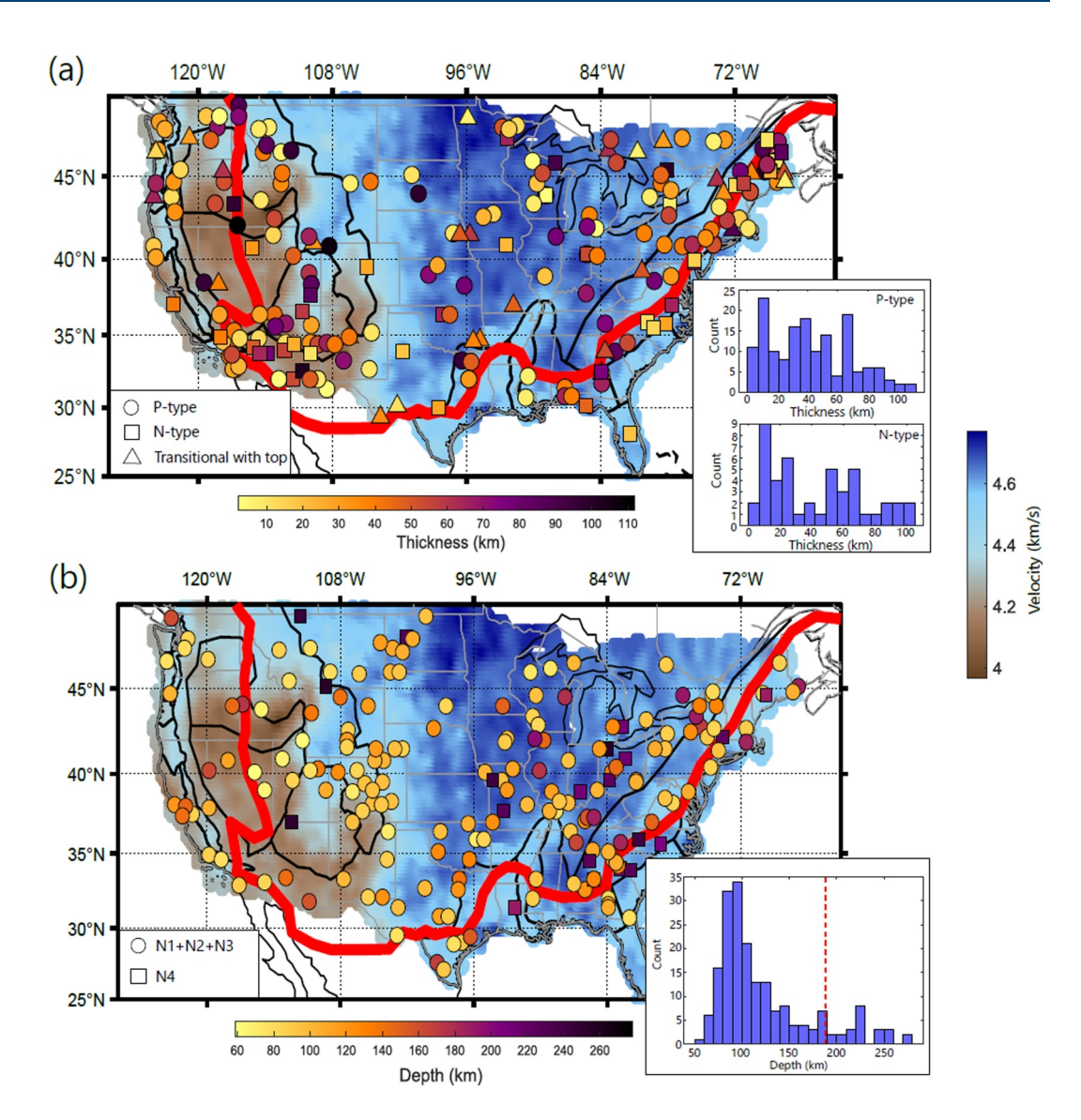


**Figure 10.** The layer thickness and depth of upper mantle stratification across the US. (a) Layer thickness below stations with paired discontinuities. The velocity change at the bottom boundary of the layer can be a velocity increase (P-type, circle) or a velocity decrease (N-type, square). For a transitional discontinuity (triangle) the top boundary is always a velocity increase. The Inset histogram shows layer thickness. (b) Depth value below stations with a single discontinuity. The Inset histogram shows depth and symbols for N1 + N2 + N3 and N4 discontinuities (compare with Figure 8). The red line marks the minimum depth for N4 discontinuities. The velocity model data is from Shen and Ritzwoller (2016).

caution to reflect more generic discontinuities associated with younger terrains (brown symbols). For simplicity, however, we retain our current taxonomy as presented.

# 5. Discussions and Interpretations

Our results, using filtered Ps-RFs, show that the upper mantle beneath the US is stratified. In the broadest sense, this view of the upper mantle's stratification, particularly within and across the lithosphere, is consistent with previous regional and continent-wide (Abt et al., 2010; Hopper & Fischer, 2018; Kind et al., 2020; Lekić & Fischer, 2014; Lekic et al., 2011; Levander & Miller, 2012; T. Liu et al., 2023) as well as single-station observations (Ford et al., 2016; Hua et al., 2023; Krueger et al., 2021; Long et al., 2017; Luo et al., 2021; Rychert et al., 2005, 2007). However, our work differs in some specific details, especially across and below the lithosphere. First, our results refine the sharpness, depth variation, and complexity of intra-lithosphere discontinuities. Second, we show that some of these discontinuities have a top and bottom boundary, while others do not. Lastly, we can show a rare

CARR AND OLUGBOJI 16 of 23

detection of a class of discontinuity transitional between the upper mantle lithosphere and asthenosphere (Kind et al., 2020) and an elusive sub-lithosphere discontinuity that might be consistent with the X-discontinuity (Pugh et al., 2021). In what follows, we: (a) provide a justification for a new taxonomy of upper mantle stratification, (b) summarize our revised constraints providing the reasoning for why our approach to mantle imaging enables a refined view of upper mantle stratification (in contrast with S-wave conversions or reflections), and (c) discuss the implications of our revised constraints for causal models for upper mantle stratification.

### 5.1. A New Taxonomy and Its Justification

In describing upper mantle structure, we introduce a new taxonomy—a way of organizing and describing how upper mantle stratification varies across the US. This new taxonomy is informed by the descriptive patterns visible in the cluster analysis (Figure 9). We observe that most of the variability in the upper mantle stratification can be organized in three main ways: (a) intra-lithosphere discontinuities (paired or single boundary), (b) transitional discontinuities (single boundary or with a top layer), and (c) sub-lithosphere discontinuities. In previous work by Abt et al. (2010), Fischer et al. (2010, 2020), Kind et al. (2015), Kumar et al. (2012), L. Liu and Gao (2018), and T. Liu and Shearer (2021) much effort has focused on detecting the MLDs using S-wave conversions or S-reverberations. Much of these observations belong to the class of mantle stratification we are calling the intra-lithosphere discontinuity with no base. This discontinuity, which is marked by a velocity decrease, has initially been disputed to be an artifact of deconvolution by Kind et al. (2020). Here, we confirm this to be a robust detection consistent with the re-analysis of Krueger et al. (2021) but now verified across a wider footprint of stations. Apart from the MLD, we observe other discontinuities internal to the lithosphere, some of which look more like layering, hence introducing a new naming scheme that captures this diversity.

For example, a recent global study conducted by Hua et al. (2023) revealed a PVG located at 150 km. They interpret this to be the base of a global molten asthenosphere layer. In our survey of the old and stable continental upper mantle, such a discontinuity is detected across the US, but this type of upper mantle stratification is more likely to be the base of an intra-lithosphere layer (Figure 10a P-type bottom boundary). Our taxonomy here is justified because when observed in stable continental US, this velocity increase is within the cold continental lithosphere and cannot be associated with the base of an asthenosphere layer (Figures 9 and 10a). In some rare cases, in the tectonically active western, US, or other younger terranes in the south and east, the thermal and shear-velocity structure may argue for a thinner lithosphere with a velocity increase reflecting the bottom of an asthenosphere layer (Hansen et al., 2015; Hopper et al., 2014; Priestley et al., 2018). Our final classification—the transitional and sub-lithosphere discontinuities—could be the same discontinuities as that called the LAB in Kind et al. (2020) or the X-discontinuity in Pugh et al. (2021) and Srinu et al. (2021). Here, we choose to use the term transitional discontinuity because it does not impose a rheological interpretation to the seismological observation without a clear model. The term sub-lithospheric discontinuity encompasses all possibilities: the Lehmann, the X-discontinuity, and other types of upper mantle stratification.

### 5.2. Revised Constraints on Upper Mantle Stratification

# 5.2.1. Re-Evaluation of UMD1+3 (Intra-Lithosphere Discontinuity With No Base)

The detection of an intra-lithosphere discontinuity with no base is most consistent with the previous observation of a mid-lithosphere discontinuity (MLD) in the eastern US, or the LAB in the west (Hopper & Fischer, 2018; Krueger et al., 2021; T. Liu & Shearer, 2021). Across the US, this discontinuity has previously been reported at a depth of 60–140 km (UMD1 and UMD3 in Figures 1b and 1c). As pointed out, our new results confirm those obtained using reflected and S-p converted body waves: SP-RFs, SS reflections (Figure 11). The confirmation of this discontinuity with our newly improved Ps-RF technique demonstrates that this type of mantle stratification is a feature that varies little with depth and is sharp enough to be visible at different wavelengths (Figures 6a, 6b, and 10b). Higher-resolution Ps-RF imaging provides the following revised constraints on this discontinuity: (a) it is more likely to be observed east of the Rockies (Figure 10 and Figure S9a in Supporting Information S1), (b) the depth is between  $100 \pm 50$  km (c) the velocity gradient is as sharp as ~10 km regardless of region (Figure 6). These constraints are important for evaluating causal models. Note also that in the west of the US the intra-lithosphere discontinuities are mostly marked by a bottom boundary, unlike to the east (Figure 10a). This observation rules out the need for a distinction between MLD and LAB and suggests that intra-lithosphere discontinuities with no base are a clear feature of cold continental lithosphere that has not been thermally

CARR AND OLUGBOJI 17 of 23

21699356, 2024, 5, Downloaded from https://agupubs.onlinelibrary.wiley.com/doi/10.1029/2024JB028781 by University Of Rochester, Wiley Online Library on [05/09/2024]. See the Terms and Conditions (https://onlinelibrary.onlinelibrary.wiley.com/doi/10.1029/2024JB028781 by University Of Rochester, Wiley Online Library on [05/09/2024]. See the Terms and Conditions (https://onlinelibrary.onlinelibrary.wiley.com/doi/10.1029/2024JB028781 by University Of Rochester, Wiley Online Library on [05/09/2024]. See the Terms and Conditions (https://onlinelibrary.onlinelibrary.wiley.com/doi/10.1029/2024JB028781 by University Of Rochester, Wiley Online Library on [05/09/2024]. See the Terms and Conditions (https://onlinelibrary.onlinelibrary.wiley.com/doi/10.1029/2024JB028781 by University Of Rochester, Wiley Online Library on [05/09/2024]. See the Terms and Conditions (https://onlinelibrary.onlinelibrary.wiley.com/doi/10.1029/2024JB028781 by University Of Rochester, Wiley Online Library on [05/09/2024]. See the Terms and Conditions (https://onlinelibrary.onlinelibrary.wiley.com/doi/10.1029/2024JB028781 by University Of Rochester, Wiley Online Library.

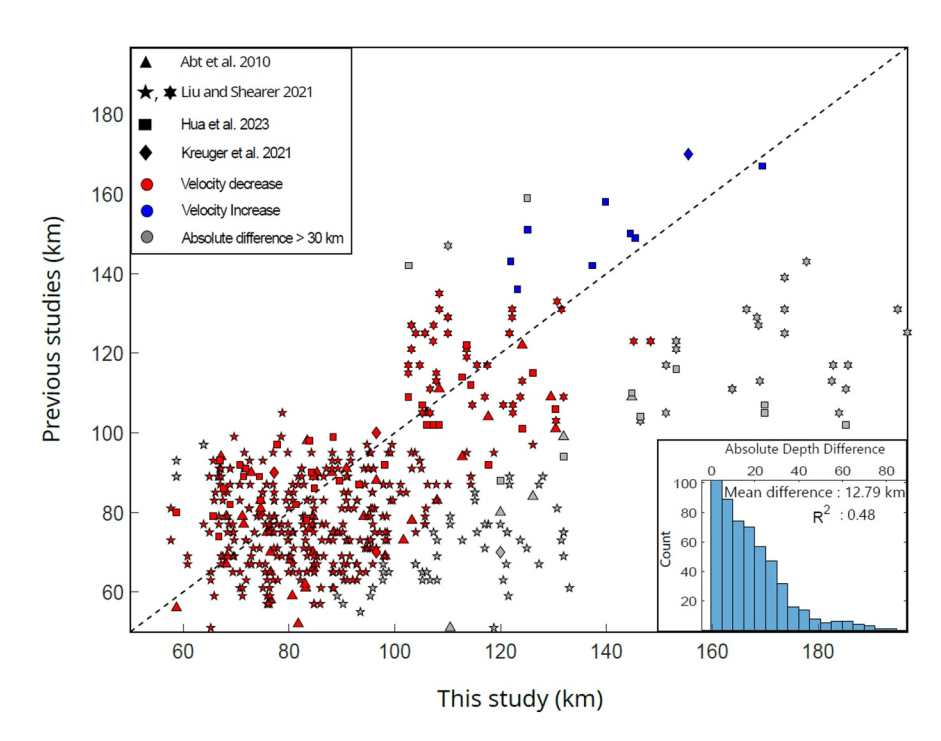


Figure 11. A comparison of previous body-wave studies of upper mantle discontinuities and this study. The scatter plot shows depth estimates for negative and positive discontinuities for similar locations. A one-to-one line (black dashed line) means that our results are consistent with previous work. Outliers are indicated in gray. The two different star symbols for T. Liu and Shearer (2021) represent data points for deep mid-lithosphere discontinuitie (MLD) (six pointed star) and shallow MLD/LAB (five pointed star) from their study. Sample filtered P-to-S receiver functions for two stations US.ECSD and IU.RSSD previously studied by Krueger et al. (2021), and T. Liu et al. (2023) can be seen in Figure S11 in Supporting Information S1.

modified over much of the US's tectonic history and yet can maintain a near-universal discontinuity that seems to be unrelated to the history of continental formation.

# 5.2.2. Re-Evaluation of UMD2 (Intra-Lithosphere Layering)

The observation of an intra-lithospheric layering with a discernible top and bottom boundary may be consistent with the PVG-150 km detected by Hua et al. (2023). However, this interpretation is only consistent for stations located to the west of the Rockies. The spatial clustering along regions with recent magmatic activity—south of the Colorado Plateau and within the Columbia River basalt suggests that in these regions alone—not in the eastern US—do you have a lithosphere that may be thermally modified in such a way as to produce a partial molten layer that results in a shallow velocity decrease with a discernible velocity increase at the bottom boundary of a rheological weak asthenosphere layer. In the eastern US, however, such an interpretation is not consistent with the observations, and a new model is required. Also, in a few locations, such as certain parts of the Basin and Range Province, we observe a more puzzling layering pattern that contradicts the partial melt interpretation - a velocity increase above a velocity decrease (N-type), Figure 10a.

### 5.3. Improved Visibility of the Transitional and X-Discontinuity

As we have seen, discontinuities internal to the lithosphere are easily detectable. However, the high-frequency body-wave signature of the boundary between a lithosphere and an asthenosphere has proved elusive beneath the Archean or Proterozoic lithosphere in the eastern US. This is probably due to the gradual thermal and compositional structure leading to the lack of a sharp boundary at a depth of 250 km (Dalton et al., 2017; Fischer et al., 2020; Priestley et al., 2018). In the continent-wide and single-station studies (Kind et al., 2020; Krueger et al., 2021; Mancinelli et al., 2017) the detections of a transitional discontinuity marked by a velocity decrease are referred to as the craton LAB and are most clearly observed by (Kind et al., 2020) in the southeastern region of the US and on craton boundaries by (Krueger et al., 2021). In our case, the detection of a deep discontinuity is rare and

CARR AND OLUGBOJI 18 of 23



# Journal of Geophysical Research: Solid Earth

10.1029/2024JB028781

spatially variable (Figure 9 and Figures S8c and S7d in Supporting Information S1). As a result, we hesitate to make any inference on the driving mechanisms for its visibility.

Similarly, PVGs have previously been detected within and beneath the lithosphere. For detections within the lithosphere, the favored interpretation is the signature of paleo-subduction beneath the Superior craton, or craton assembly through imbrication and underplating (Kind et al., 2020). Although we observe these discontinuities in the lithosphere, the spatial resolution is not high enough to place constraints on their tectonic drivers. Most of our detections are associated with the top or bottom boundary of a lithospheric layer rather than a structural feature of continental assembly. The most compelling observation is the rare detections of sub-lithosphere discontinuities at 250–300 km (Figures S6c and S8c in Supporting Information S1). We interpret these as an X-discontinuity similar to that seen globally by Pugh et al. (2021). The similarity between previously reported results and ours, that is velocity increases at similar depths, lends further strength to this interpretation (Pugh et al., 2021, 2023) (Figure S8c in Supporting Information S1). We note that the interpretation of a shallower positive discontinuity as the Lehmann discontinuity is not supported by our results. Some authors have argued that the Lehmann discontinuity is caused by anisotropy (Gaherty & Jordan, 1995; Gung et al., 2003). Since the current version of our Radon technique assumes an isotropic Earth model it is not suited for resolving anisotropic stratification. Future work is needed to evaluate if this discontinuity is preferably associated with anisotropy.

### 5.4. A Case for Models Consistent With Revised Constraints

Based on our new constraints we re-evaluate the different models proposed to explain intra-lithosphere and transitional discontinuities (Karato & Park, 2018; H. Yuan & Romanowicz, 2018). They include partial melting (Golos & Fischer, 2022; Hua et al., 2023; Rader et al., 2015) chemical stratification or metasomatism (Krueger et al., 2021; T. Liu et al., 2023; Rader et al., 2015; Saha et al., 2021; Selway et al., 2015), variable anisotropy (Wirth & Long, 2014; H. Yuan & Levin, 2014; H. Yuan & Romanowicz, 2010), and elastically accommodated grain-boundary sliding (Karato et al., 2015). Many of these models were proposed shortly after the early detection of lithosphere discontinuities when a detailed view of upper mantle stratification was unavailable. The new observations suggest that some models are more consistent with discontinuities without a base while others are more consistent with those with a base.

### 5.4.1. Intra-Lithosphere Discontinuities With No Base

The simplest class of mantle stratification is the intra-lithospheric discontinuity with no base. This discontinuity, more likely to be observed in cold continental lithosphere, has a very systematic behavior that makes it hard to reconcile with models that prescribe a unique tectonic history—for example, metasomatism or imbrication and underplating during craton assembly. For example, a discontinuity that is relatively sharp with no bottom boundary and is more likely to be observed east of the Rockies at a depth that varies systematically: the shallowest discontinuities (60 km) in the west and deepest (135 km) in the east. This near-universal discontinuity in the cold continental lithosphere leads us to prefer the attenuation-related model of Karato et al. (2015) for this class of mantle stratification. As conceived, this model can reduce velocities across the US at sub-solidus temperatures either through thermal relaxation or hydration, without the need for a deeper increase in velocities, ruling out the need for a bottom base. The depth dependence of temperature and hydration in the grain-boundary sliding model can explain the deepening of this discontinuity. It is hard to reconcile this observation with the metasomatic model.

# 5.4.2. Intra-Lithosphere Layering With a Top and Bottom Boundary

The second class of mantle stratification is the intra-lithospheric discontinuity with a top and bottom boundary. In this class, the easiest to explain is the P-type boundary—a velocity increase below a velocity decrease. Because this discontinuity is more likely to be observed in the tectonically active and recently magmatic regions or along the Appalachians, we are inclined to prefer the partial melt or metasomatic model to explain this class of mantle stratification. If the lithosphere is significantly thermally perturbed, with the infusion, into the mantle, of low-velocity iron-rich or fluid-rich minerals, partial melting or metasomatism might lead to a reduction in velocity, below which an increase in velocity, detected as a bottom base, will be observed (Karato & Park, 2018; Saha et al., 2021). The reason why this bottom base has gone undetected until now might be related to the low-frequency content of Sp-RFs with or without deconvolution (Kind & Yuan, 2018; X. Yuan et al., 2006)

CARR AND OLUGBOJI 19 of 23

compared to the higher-resolution Ps-RFs or anisotropy (Olugboji et al., 2013; Olugboji, Zhang, et al., 2023). Also, in the S-reflection technique used by (T. Liu & Shearer, 2021; T. Liu et al., 2023) the resolution is limited to shallow discontinuities (<150 km) due to the ambiguity of distinguishing source-side and receiver-side reflections. The N-type boundary—velocity decrease below a velocity increase is harder to explain. One simple model is that this reflects relics of craton assembly or crustal underplating. A thickened crust, or subducted lithosphere embedded within a lower velocity layer is one way to explain this observation. The geological preference for regions where such a tectonic scenario can be envisioned is another reason for our preference for this model.

### 5.4.3. Transitional Discontinuities and the X

The final class of mantle stratification is transitional and sub-lithosphere discontinuities. Strictly speaking, these discontinuities are of different types and are rare: negative velocity gradients for the transition across a lithosphere to asthenosphere transition and a PVG for the sub-lithosphere discontinuity. For the discontinuity associated with the lithosphere-asthenosphere transition, the current statistics suggest that this discontinuity is more likely to be observed in the cold continental lithosphere in the eastern US (Figure 9 and Figure S8c in Supporting Information S1). The sparsity of observations should be related to the small velocity decrease at these depths due to weak thermal and compositional gradients at these depths (Fischer et al., 2010). The rarity of the sub-lithosphere X-discontinuity at 300 km is also a clear indication that phase transformations or recycling of basalts at hotspots are very unlikely across the US (Figure S8c in Supporting Information S1).

### 5.5. Current Limits, Next Steps: Hales, Lehmann, and Anisotropy

In our current assessment of upper mantle stratification, the CRISP-RF approach has produced a higher-resolution and improved view of upper mantle stratification. This success is due to improvements in frequency content as well as the availability of long-running stations that allow for wavefield separation of deep mantle conversions from shallow crustal reverberations. Despite these improvements, our taxonomy of upper mantle stratification does not yet explore anisotropy as do some recent studies using anisotropic Ps-RFs (Abt et al., 2010; Ford et al., 2016; Levin et al., 2023; Park & Levin, 2016a; Wirth & Long, 2014; H. Yuan & Levin, 2014). This is because the radon-transformed Ps-RFs we use assume isotropic layering. A generalization of the CRISP-RF methodology to investigate anisotropy is a natural next step. We do argue that in future generalization of our methodology to investigating anisotropy, back-azimuthal harmonic decomposition, as described in (Bostock, 1997, 1998; Levin & Park, 1998; Park & Levin, 2016c) should be applied only after isotropic layer-stripping and attenuation of crustal reverberations using CRISP-RF. An improved method for investigating anisotropy not contaminated by shallow crustal reverberations will allow us to evaluate models that invoke anisotropy for both intra-lithosphere and sub-lithosphere discontinuities, for example, Lehmann, Hales, and Gutenberg discontinuities (Deuss, 2009; Deuss & Woodhouse, 2004; Ford et al., 2016; Gaherty & Jordan, 1995; Gung et al., 2003)

### 6. Conclusions

The upper mantle structure beneath the US is investigated using high-resolution Ps-converted waves after filtering out shallow crustal reverberations. After careful data curation, using 417 of the best stations that span a diversity of physiographic provinces, followed by polarity-dependent filtering, sequencing, and clustering, we obtain a new and improved taxonomy of upper mantle stratification. We observe that the most dominant type of upper mantle stratification (84% of station inventory) is within the lithosphere—about half of which are discontinuities without a base and the other half are layers with a top and bottom boundary. A re-evaluation of causal models based on our revised constraints suggests that some class of models better explain the former than they do the latter. The remainder of our stations (16%) show rare detections of discontinuities transitional between the lithosphere and the asthenosphere and an X-type sub-lithosphere discontinuity. This suggests a limited role of such discontinuities in explaining upper mantle stratification. Future work should verify our results on a global scale and revisit the evaluation of causal models, especially with regards to anisotropy.

CARR AND OLUGBOJI 20 of 23

# **Data Availability Statement**

The waveform data used in this study can be retrieved from the Seismological Facility for the Advancement of Geoscience (SAGE)/EarthScope Data Management System using Obspy's routines for mass download (IRIS Transportable Array, 2003). The codes and results for waveform processing is accessible in Carr and Olugboji (2024). The repository contains all metadata information, Ps-RF results and station classification.

### Acknowledgments

This work was made possible by a seed grant from the University of Rochester's Goergen Institute for Data Science and support from the National Science Foundation under Grant 1818654. The authors acknowledge the use of the BlueHive Linux cluster at the University of Rochester's Center for Integrated Research Computing, CIRC (https://www.circ. rochester.edu/). The authors acknowledge many helpful discussions with Vedran Lekic, Nicholas Schmerr, Lara Wagner, Baowei Liu, Jeffrey Park, Shun-ichiro Karato, Gary Egbert, Joseph Byrnes, Eva Golos, and the Associate Editor. The manuscript was significantly improved by helpful comments from Shun-ichiro Karato.

### References

- Abt, D. L., Fischer, K. M., French, S. W., Ford, H. A., Yuan, H., & Romanowicz, B. (2010). North American lithospheric discontinuity structure imaged by Ps and Sp receiver functions. *Journal of Geophysical Research*, 115(B9), B09301. https://doi.org/10.1029/2009jb006914Baron, D., & Ménard, B. (2020). Extracting the main trend in a dataset: The sequencer algorithm.
- Beck, A., & Teboulle, M. (2009). A fast iterative Shrinkage-Thresholding algorithm for linear inverse problems. SIAM Journal on Imaging Sciences, 2(1), 183–202. https://doi.org/10.1137/080716542
- Bostock, M. G. (1997). Anisotropic upper-mantle stratigraphy and architecture of the slave craton. *Nature*, 390(6658), 392–395. https://doi.org/10.1038/37102
- Bostock, M. G. (1998). Mantle stratigraphy and evolution of the slave province. *Journal of Geophysical Research: Solid Earth*, 103(B9), 21183–21200. https://doi.org/10.1029/98jb01069
- Carlson, R. W., Pearson, D. G., & James, D. E. (2005). Physical, chemical, and chronological characteristics of continental mantle. *Reviews of Geophysics*, 43(1), RG1001, https://doi.org/10.1029/2004re000156
- Geophysics, 43(1), RG1001. https://doi.org/10.1029/2004rg000156
  Carr, S., & Olugboji, T. (2024). Urseismology/usmantletax: Preprint release [Software]. Zenodo. https://doi.org/10.5281/zenodo.10849716
- Chen, C., Gilbert, H., Fischer, K. M., Andronicos, C. L., Pavlis, G. L., Hamburger, M. W., et al. (2018). Lithospheric discontinuities beneath the U. S. midcontinent—Signatures of Proterozoic terrane accretion and failed rifting. *Earth and Planetary Science Letters*, 481, 223–235. https://doi.org/10.1016/j.epsl.2017.10.033
- Dalton, C. A., Bao, X., & Ma, Z. (2017). The thermal structure of cratonic lithosphere from global Rayleigh wave attenuation. Earth and Planetary Science Letters, 457, 250–262. https://doi.org/10.1016/j.epsl.2016.10.014
- Deuss, A. (2009). Global observations of mantle discontinuities using SS and PP precursors. Surveys in Geophysics, 30(4–5), 301–326. https://doi.org/10.1007/s10712-009-9078-y
- Deuss, A., & Woodhouse, J. H. (2004). The nature of the Lehmann discontinuity from its seismological clapeyron slopes. *Earth and Planetary Science Letters*, 225(3), 295–304. https://doi.org/10.1016/j.epsl.2004.06.021
- Dziewonski, A. M., & Anderson, D. L. (1981). Preliminary reference Earth model. *Physics of the Earth and Planetary Interiors*, 25(4), 297–356. https://doi.org/10.1016/0031-9201(81)90046-7
- https://doi.org/10.1016/0031-9201(81)90046-7
  Eaton, D. W., Darbyshire, F., Evans, R. L., Grütter, H., Jones, A. G., & Yuan, X. (2009). The elusive lithosphere–asthenosphere boundary (LAB)
- beneath cratons. Lithos, 109(1), 1–22. https://doi.org/10.1016/j.lithos.2008.05.009

  Fang, H. (2024). Sequencing seismic noise correlations for improving surface wave retrieval and characterizing noise sources. Seismological Research Letters. 95(2A), 848–858. https://doi.org/10.1785/0220230151
- Fischer, K. M., Ford, H. A., Abt, D. L., & Rychert, C. A. (2010). The lithosphere-asthenosphere boundary. *Annual Review of Earth and Planetary Sciences*, 38(1), 551–575. https://doi.org/10.1146/annurev-earth-040809-152438
- Fischer, K. M., Rychert, C. A., Dalton, C. A., Miller, M. S., Beghein, C., & Schutt, D. L. (2020). A comparison of oceanic and continental mantle lithosphere. *Physics of the Earth and Planetary Interiors*, 309, 106600. https://doi.org/10.1016/j.pepi.2020.106600
- Ford, H. A., Long, M. D., & Wirth, E. A. (2015). Characterizing azimuthal anisotropy at the mid-lithospheric discontinuity in the superior and Wyoming cratons. In AGU fall meeting abstracts (Vol. 2015, pp. DI24A-01). ui.adsabs.harvard.edu.
- Ford, H. A., Long, M. D., & Wirth, E. A. (2016). Midlithospheric discontinuities and complex anisotropic layering in the mantle lithosphere beneath the Wyoming and superior provinces. *Journal of Geophysical Research: Solid Earth*, 121(9), 6675–6697. https://doi.org/10.1002/
- Gaherty, J. B., & Jordan, T. H. (1995). Lehmann discontinuity as the base of an anisotropic layer beneath continents. *Science*, 268(5216), 1468–1471. https://doi.org/10.1126/science.268.5216.1468
- Golos, E. M., & Fischer, K. M. (2022). New insights into lithospheric structure and melting beneath the Colorado Plateau. Geochemistry, Geophysics, Geosystems, 23(3), e2021GC010252. https://doi.org/10.1029/2021gc010252
- Gong, X., Yu, S., & Wang, S. (2016). Prestack seismic data regularization using a time-variant anisotropic radon transform. *Journal of Geophysics and Engineering*, 13(4), 462–469. https://doi.org/10.1088/1742-2132/13/4/462
- Guan, Z., & Niu, F. (2017). An investigation on slowness-weighted CCP stacking and its application to receiver function imaging. *Geophysical Research Letters*, 44(12), 6030–6038. https://doi.org/10.1002/2017gl073755
- Gung, Y., Panning, M., & Romanowicz, B. (2003). Global anisotropy and the thickness of continents. Nature, 422(6933), 707–711. https://doi.org/10.1038/nature01559
- Hansen, S. M., Dueker, K., & Schmandt, B. (2015). Thermal classification of lithospheric discontinuities beneath USArray. Earth and Planetary Science Letters, 431, 36–47. https://doi.org/10.1016/j.epsl.2015.09.009
- Helffrich, G. (2006). Extended-time multitaper frequency domain cross-correlation receiver-function estimation. Bulletin of the Seismological Society of America, 96(1), 344–347. https://doi.org/10.1785/0120050098
- Hopper, E., & Fischer, K. M. (2018). The changing face of the lithosphere-asthenosphere boundary: Imaging continental scale patterns in upper mantle structure across the contiguous US with Sp converted waves. *Geochemistry, Geophysics, Geosystems*, 19(8), 2593–2614. https://doi. org/10.1029/2018gc007476
- Hopper, E., Ford, H. A., Fischer, K. M., Lekic, V., & Fouch, M. J. (2014). The lithosphere–asthenosphere boundary and the tectonic and magmatic history of the northwestern United States. Earth and Planetary Science Letters, 402, 69–81. https://doi.org/10.1016/j.epsl.2013.12.016
- Hosseini, K., Sigloch, K., Tsekhmistrenko, M., Zaheri, A., Nissen-Meyer, T., & Igel, H. (2019). Global mantle structure from multifrequency tomography using p, PP and p-diffracted waves. Geophysical Journal International, 220(1), 96–141. https://doi.org/10.1093/gji/ggz394
- Hua, J., Fischer, K. M., Becker, T. W., Gazel, E., & Hirth, G. (2023). Asthenospheric low-velocity zone consistent with globally prevalent partial melting. *Nature Geoscience*, 16(2), 175–181. https://doi.org/10.1038/s41561-022-01116-9
- IRIS Transportable Array. (2003). Usarray transportable array [Dataset]. International Federation of Digital Seismograph Networks. https://doi.org/10.7914/SN/TA

CARR AND OLUGBOJI 21 of 23



# Journal of Geophysical Research: Solid Earth

- 10.1029/2024JB028781
- Karato, S.-I. (2012). On the origin of the asthenosphere. Earth and Planetary Science Letters, 321–322, 95–103. https://doi.org/10.1016/j.epsl.
- Karato, S.-I., Olugboji, T., & Park, J. (2015). Mechanisms and geologic significance of the mid-lithosphere discontinuity in the continents. *Nature Geoscience*, 8(7), 509–514. https://doi.org/10.1038/ngeo2462
- Karato, S.-I., & Park, J. (2018). On the origin of the upper mantle seismic discontinuities. In H. Yuan, & B. Romanowicz (Eds.), Lithospheric discontinuities (Vol. 115, pp. 5–34). John Wiley and Sons, Inc. https://doi.org/10.1002/9781119249740.ch1
- Kim, D., Lekić, V., Ménard, B., Baron, D., & Taghizadeh-Popp, M. (2020). Sequencing seismograms: A panoptic view of scattering in the coremantle boundary region. Science, 368(6496), 1223–1228. https://doi.org/10.1126/science.aba8972
- Kind, R., Mooney, W. D., & Yuan, X. (2020). New insights into the structural elements of the upper mantle beneath the contiguous United States from S-to-P converted seismic waves. *Geophysical Journal International*, 222(1), 646–659. https://doi.org/10.1093/gji/ggaa203
- Kind, R., & Yuan, X. (2018). Perspectives of the S -receiver-function method to image upper mantle discontinuities. In *Lithospheric discontinuities* (pp. 139–154). John Wiley and Sons, Inc.
- Kind, R., Yuan, X., & Kumar, P. (2012). Seismic receiver functions and the lithosphere–asthenosphere boundary. *Tectonophysics*, 536–537, 25–43. https://doi.org/10.1016/j.tecto.2012.03.005
- Kind, R., Yuan, X., Mechie, J., & Sodoudi, F. (2015). Structure of the upper mantle in the north-western and central United States from USArray S-receiver functions. *Solid Earth*, 6(3), 957–970. https://doi.org/10.5194/se-6-957-2015
- Krueger, H. E., Gama, I., & Fischer, K. M. (2021). Global patterns in cratonic mid-lithospheric discontinuities from Sp receiver functions. Geochemistry, Geophysics, Geosystems, 22(6), e2021GC009819. https://doi.org/10.1029/2021gc009819
- Kumar, P., Kind, R., Yuan, X., & Mechie, J. (2012). USArray receiver function images of the lithosphere-asthenosphere boundary. Seismological Research Letters, 83(3), 486–491. https://doi.org/10.1785/gssrl.83.3.486
- Langston, C. A. (1977). Corvallis, Oregon, crustal and upper mantle receiver structure from teleseismic P and S waves. Bulletin of the Seismological Society of America, 67(3), 713–724. https://doi.org/10.1785/bssa0670030713
- Lekić, V., & Fischer, K. M. (2014). Contrasting lithospheric signatures across the western United States revealed by Sp receiver functions. Earth and Planetary Science Letters, 402, 90–98. https://doi.org/10.1016/j.epsl.2013.11.026
- Lekic, V., French, S. W., & Fischer, K. M. (2011). Lithospheric thinning beneath rifted regions of southern California. *Science*, 334(6057), 783–787. https://doi.org/10.1126/science.1208898
- Levander, A., & Miller, M. S. (2012). Evolutionary aspects of lithosphere discontinuity structure in the western U.S. Geochemistry, Geophysics, Geosystems, 13(7), Q0AK07. https://doi.org/10.1029/2012gc004056
- Levin, V., Lebedev, S., Fullea, J., Li, Y., & Chen, X. (2023). Defining continental lithosphere as a layer with abundant frozen-in structures that scatter seismic waves. *Journal of Geophysical Research: Solid Earth*, 128(7), e2022JB026309. https://doi.org/10.1029/2022jb026309
- Levin, V., & Park, J. (1998). P-SH conversions in layered media with hexagonally symmetric anisotropy: A CookBook. In *Geodynamics of*
- lithosphere and Earth's mantle (pp. 669–697). Birkhäuser Basel. Liu, L., & Gao, S. S. (2018). Lithospheric layering beneath the contiguous United States constrained by S-to-P receiver functions. Earth and
- Planetary Science Letters, 495, 79–86. https://doi.org/10.1016/j.epsl.2018.05.012
  Liu, T., Chin, E. J., & Shearer, P. (2023). Strong physical contrasts across two mid-lithosphere discontinuities beneath the northwestern United
- States: Evidence for cratonic mantle metasomatism. AGU Advances, 4(6), e2023AV001014. https://doi.org/10.1029/2023av001014 Liu, T., & Shearer, P. M. (2021). Complicated lithospheric structure beneath the contiguous US revealed by teleseismic s-reflections. Journal of
- Geophysical Research: Solid Earth, 126(5), e2020JB021624. https://doi.org/10.1029/2020jb021624 Long, M. D., Ford, H. A., Abrahams, L., & Wirth, E. A. (2017). The seismic signature of lithospheric deformation beneath eastern North America
- due to Grenville and Appalachian orogenesis. *Lithosphere*, 9(6), 987–1001. https://doi.org/10.1130/1660.1 Luo, Y., Long, M. D., Karabinos, P., Kuiper, Y. D., Rondenay, S., Aragon, J. C., et al. (2021). High-resolution Ps receiver function imaging of the
- crust and mantle lithosphere beneath southern New England and tectonic implications. *Journal of Geophysical Research: Solid Earth*, 126(7), e2021JB022170. https://doi.org/10.1029/2021jb022170

  Mancinelli, N. J., Fischer, K. M., & Dalton, C. A. (2017). How sharp is the cratonic lithosphere-asthenosphere transition? *Geophysical Research*
- Mancinelli, N. J., Fischer, K. M., & Dalton, C. A. (2017). How sharp is the cratonic lithosphere-asthenosphere transition? *Geophysical Research Letters*, 44(20), 10189–10197. https://doi.org/10.1002/2017gl074518
- Olugboji, T., Xue, S., Legre, J.-J., & Tamama, Y. (2023). Africa's crustal architecture inferred from probabilistic and perturbational inversion of ambient noise: Adama.
- Olugboji, T., Zhang, Z., Carr, S., Ekmekci, C., & Cetin, M. (2023). On the detection of upper mantle discontinuities with radon-transformed receiver functions (CRISP-RF). *Geophysical Journal International*, 236(2), 748–763. https://doi.org/10.1093/gji/ggad447
- Olugboji, T. M., Karato, S., & Park, J. (2013). Structures of the oceanic lithosphere-asthenosphere boundary: Mineral-physics modeling and seismological signatures. *Geochemistry, Geophysics, Geosystems*, 14(4), 880–901. https://doi.org/10.1002/ggge.20086
- Park, J., & Levin, V. (2000). Receiver functions from multiple-taper spectral correlation estimates. Bulletin of the Seismological Society of America, 90(6), 1507–1520. https://doi.org/10.1785/0119990122
- Park, J., & Levin, V. (2016a). Anisotropic shear zones revealed by backazimuthal harmonics of teleseismic receiver functions. *Geophysical Supplements to the Monthly Notices of the Royal Astronomical Society*, 207(2), 1216–1243. https://doi.org/10.1093/gji/ggw323
- Park, J., & Levin, V. (2016b). Receiver functions from multiple-taper spectral correlation: Statistics, single-station migration, and jackknife uncertainty. Geophysical Journal International, 207(1), 512–527. https://doi.org/10.1093/gji/ggw291
- Park, J., & Levin, V. (2016c). Statistics and frequency-domain moveout for multiple-taper receiver functions. Geophysical Journal International, 207(1), 512–527. https://doi.org/10.1093/gji/ggw291
- Priestley, K., McKenzie, D., & Ho, T. (2018). A lithosphere-asthenosphere boundary-a global model derived from multimode surface-wave tomography and petrology. In *Lithospheric discontinuities* (pp. 111–123). John Wiley and Sons, Inc.
- Pugh, S., Boyce, A., Bastow, I. D., Ebinger, C. J., & Cottaar, S. (2023). Multigenetic origin of the x-discontinuity below continents: Insights from African receiver functions. *Geochemistry, Geophysics, Geosystems*, 24(3), e2022GC010782. https://doi.org/10.1029/2022gc010782
- Pugh, S., Jenkins, J., Boyce, A., & Cottaar, S. (2021). Global receiver function observations of the x-discontinuity reveal recycled basalt beneath hotspots. Earth and Planetary Science Letters, 561, 116813. https://doi.org/10.1016/j.epsl.2021.116813
- Rader, E., Emry, E., Schmerr, N., Frost, D., Cheng, C., Menard, J., et al. (2015). Characterization and petrological constraints of the midlithospheric discontinuity. Geochemistry, Geophysics, Geosystems, 16(10), 3484–3504. https://doi.org/10.1002/2015gc005943
- Rondenay, S. (2009). Upper mantle imaging with array recordings of converted and scattered teleseismic waves. Surveys in Geophysics, 30(4), 377–405. https://doi.org/10.1007/s10712-009-9071-5
- Ryberg, T., & Weber, M. (2000). Receiver function arrays: A reflection seismic approach. *Geophysical Journal International*, 141(1), 1–11. https://doi.org/10.1046/j.1365-246x.2000.00077.x

CARR AND OLUGBOJI 22 of 23



# Journal of Geophysical Research: Solid Earth

- 10.1029/2024JB028781
- Rychert, C. A., Fischer, K. M., & Rondenay, S. (2005). A sharp lithosphere–asthenosphere boundary imaged beneath eastern North America. Nature, 436(7050), 542–545, https://doi.org/10.1038/nature03904
- Rychert, C. A., Rondenay, S., & Fischer, K. M. (2007). P -to- S and S -to- P imaging of a sharp lithosphere-asthenosphere boundary beneath eastern North America. *Journal of Geophysical Research*, 112(B8), B08314. https://doi.org/10.1029/2006JB004619
- Saha, S., Peng, Y., Dasgupta, R., Mookherjee, M., & Fischer, K. M. (2021). Assessing the presence of volatile-bearing mineral phases in the cratonic mantle as a possible cause of mid-lithospheric discontinuities. *Earth and Planetary Science Letters*, 553, 116602. https://doi.org/10.1016/j.epsl.2020.116602
- Schmandt, B., Lin, F.-C., & Karlstrom, K. E. (2015). Distinct crustal isostasy trends east and west of the Rocky Mountain Front. *Geophysical Research Letters*, 42(23), 10–290. https://doi.org/10.1002/2015gl066593
- Selway, K., Ford, H., & Kelemen, P. (2015). The seismic mid-lithosphere discontinuity. Earth and Planetary Science Letters, 414, 45–57. https://doi.org/10.1016/j.epsl.2014.12.029
- Shearer, P. M., & Buehler, J. (2019). Imaging upper-mantle structure under USArray using long-period reflection seismology. *Journal of Geophysical Research: Solid Earth*, 124(9), 9638–9652. https://doi.org/10.1029/2019jb017326
- Shen, W., & Ritzwoller, M. H. (2016). Crustal and uppermost mantle structure beneath the United States. *Journal of Geophysical Research: Solid Earth*, 121(6), 4306–4342. https://doi.org/10.1002/2016jb012887
- Shi, J., Wang, T., & Chen, L. (2020). Receiver function velocity analysis technique and its application to remove multiples. *Journal of Geophysical Research: Solid Earth*, 125(8), e2020JB019420. https://doi.org/10.1029/2020jb019420
- Shi, Y.-N., & Morgan, J. P. (2022). Plume-lithosphere interaction and delamination at Yellowstone and its implications for the boundary of craton stability. *Geophysical Research Letters*, 49(2), e2021GL096864, https://doi.org/10.1029/2021gl096864
- Shibutani, T., Ueno, T., & Hirahara, K. (2008). Improvement in the extended-time multitaper receiver function estimation technique. Bulletin of the Seismological Society of America, 98(2), 812–816. https://doi.org/10.1785/0120070226
- Srinu, U., Kumar, P., Haldar, C., Kumar, M. R., Srinagesh, D., & Illa, B. (2021). X-discontinuity beneath the Indian Shield—Evidence for remnant Tethyan oceanic lithosphere in the mantle. *Journal of Geophysical Research: Solid Earth*, 126(8), e2021JB021890. https://doi.org/10.1029/2021jb021890
- Stähler, S. C., Sigloch, K., & Nissen-Meyer, T. (2012). Triplicated P-wave measurements for waveform tomography of the mantle transition zone. Solid Earth Discuss. 4(2), 783–821.
- Tauzin, B., van der Hilst, R. D., Wittlinger, G., & Ricard, Y. (2013). Multiple transition zone seismic discontinuities and low velocity layers below western United States. *Journal of Geophysical Research: Solid Earth, 118*(5), 2307–2322. https://doi.org/10.1002/jgrb.50182
- Whitmeyer, S. J., & Karlstrom, K. E. (2007). Tectonic model for the Proterozoic growth of North America. Geosphere, 3(4), 220–259. https://doi.org/10.1130/ges00055.1
- Wirth, E. A., & Long, M. D. (2014). A contrast in anisotropy across mid-lithospheric discontinuities beneath the central United States—A relic of craton formation. *Geology*, 42(10), 1–4. https://doi.org/10.1130/g35804.1
- Yuan, H., & Levin, V. (2014). Stratified seismic anisotropy and the lithosphere-asthenosphere boundary beneath eastern North America. *Journal of Geophysical Research: Solid Earth*, 119(4), 3096–3114. https://doi.org/10.1002/2013jb010785
- Yuan, H., & Romanowicz, B. (2010). Lithospheric layering in the North American craton. Nature, 466(7310), 1063–1068. https://doi.org/10.1038/nature09332
- Yuan, H., & Romanowicz, B. (2018). Introduction-Lithospheric discontinuities.
- Yuan, X., Kind, R., Li, X., & Wang, R. (2006). The S receiver functions: Synthetics and data example. *Geophysical Journal International*, 165(2), 555–564. https://doi.org/10.1111/j.1365-246X.2006.02885.x

CARR AND OLUGBOJI 23 of 23